POLITECNICO DI TORINO
Repository ISTITUZIONALE

An overview on modelling approaches for photochemical and photoelectrochemical solar fuels processes and technologies

Original
An overview on modelling approaches for photochemical and photoelectrochemical solar fuels processes and technologies / Falciani, Gabriele; Chiavazzo, Eliodoro. - In: ENERGY CONVERSION AND MANAGEMENT. - ISSN 0196-8904. - ELETTRONICO. - 292:(2023). [10.1016/j.enconman.2023.117366]

Availability:
This version is available at: 11583/2980374 since: 2023-07-15T13:46:57Z

Publisher:
Elsevier

Published
DOI:10.1016/j.enconman.2023.117366

Terms of use:

This article is made available under terms and conditions as specified in the corresponding bibliographic description in the repository

Publisher copyright

(Article begins on next page)

27 April 2024

Energy Conversion and Management 292 (2023) 117366

Contents lists available at ScienceDirect

Energy Conversion and Management

journal homepage: www.elsevier.com/locate/enconman

Review

An overview on modelling approaches for photochemical and photoelectrochemical solar fuels processes and technologies

Gabriele Falciani, Eliodoro Chiavazzo *

Department of Energy, Politecnico di Torino, Torino, 10129, Italy

ARTICLE INFO

Keywords:
Multi-scale modeling
Solar fuels
Photocatalysis
Photoelectrocatalysis
Self-assembling

ABSTRACT

Photo-electrochemical and photocatalytic technologies are promising solutions for solar fuel production and involve a number of physical and chemical phenomena. We provide an overview of numerical and analytical tools to describe such phenomena occurring at disparate time and space scales within devices such as photo-electrochemical cells and photo-chemical reactors. On one hand, chemical phenomena include photo-induced electron transfer, charge separation, recombination, equilibrium reactions between species in solutions and adsorption reactions. On the other hand, examples of physical phenomena are the transport of chemical species or self-assembling of molecular structures. In this respect, we critically review macroscale continuum models for transport phenomena combined with kinetic descriptions including their possible coupling with models at even lower scales. We specifically focus on atomistic and coarse-grained models able to represent the local environment of the reactive interfaces such as photoelectrodes or supra-molecular assemblies. The critical role of the latter structures on photochemical conversion is highlighted: Therefore, morphological structure of self-assemblies, such as micelles and monolayers, in solution and at the solid–liquid or gas–liquid interfaces are also discussed. Finally, important scientific gaps are identified and possible perspectives for future research outlooked.

1. Solar fuel production processes

Global population growth and rising energy demand pose significant challenges to a sustainable future [1]. The use of fossil fuels and the emission of greenhouse gases, particularly carbon dioxide, into the atmosphere are major contributors to climate change [2]. The world energy demand is expected to double by 2050 and triple by the end of the twenty-first century [3]. Both policymakers and the general public are concerned about the depletion of fossil fuels, the environmental consequences of their use and importantly possible mitigations actions [4]. Hence, a significant shift in the global energy consumption mix is needed in the upcoming years, inducing scientists and engineers to search for zero-carbon, renewable energy sources such as wind, solar, hydropower, and geothermal to fulfill this energy demand [5,6]. Synthetic fuels generated from renewable sources can be one of the possible solutions to decrease the impact of our society on the environment [7,8]. An obvious choice to produce synthetic fuels is to exploit solar energy, which has an enormous potential as a clean, abundant, and economical energy source [9–11]. The generated solar fuel would be an energy vector able to overcome the main problem related to solar energy, namely its intermittency [12]. Hydrogen is one of the possible solar fuels and can be obtained from water splitting reducing protons while oxidizing water [13–15]. It has the highest energy density among the fuels (120 MJ/kg) and when burnt generates H_2O as byproduct. Moreover, it can be used in existing internal combustion engines, fuel cells and gas turbines [16]. However, being the lightest element, both its storage and distribution are challenging [17]. As a complementary approach, researchers have focused their efforts in using CO_2 as a potential resource to be converted in carbon based fuels, from which also carbon based chemicals can be obtained [7,18]. Indeed, carbon, capture, storage and utilization technologies are receiving an increasing attention [19].

CO_2 is a thermodynamically stable and chemically inert molecule. This makes the reduction of CO_2 a challenging process due to both thermodynamics and kinetics [20]. Multiple electron (and proton) transfers are required in order to reduce CO_2 to valuable products through several radical intermediates [21]. A possible first step in the carbon dioxide reduction process is the addition of a single electron to the CO_2 molecule which causes a bending of the linear molecular structure owing to the repulsion of the acquired electron located on the carbon atom and the free electron pairs on the two oxygen atoms. This configuration makes the anion radical $CO_2^{-\cdot}$ highly energetic. Indeed, the single-electron reduction of CO_2 has a strongly negative

* Corresponding author.
E-mail address: eliodoro.chiavazzo@polito.it (E. Chiavazzo).

https://doi.org/10.1016/j.enconman.2023.117366
Received 6 April 2023; Received in revised form 29 June 2023; Accepted 30 June 2023
Available online 14 July 2023
0196-8904/© 2023 The Author(s). Published by Elsevier Ltd. This is an open access article under the CC BY license (http://creativecommons.org/licenses/by/4.0/).

Nomenclature

$[P]$	Concentration of the products
$[PC]$	Concentration of the photocatalyst in the ground state
$[PC^*]$	Concentration of the photocatalyst in the excited state
$[PC^+]$	Concentration of the photocatalyst in the oxidized state
$[PC_0]$	Concentration of the photocatalyst in all states
$[S]$	Concentration of the reactant
$[S_1]$	Concentration of the reactant 1
$[S_2]$	Concentration of the reactant 2
α	Coefficient which considers the head group interactions
$\alpha(\lambda)$	Absorption coefficient of the mean
α_a	Charge transfer coefficient of the anodic reaction
α_c	Charge transfer coefficient of the cathodic reaction
β	Coefficient which considers the interactions between adsorbed molecules
ΔU	Energy variation of the system before and after the addition, translation or deletion move
ΔV_{Nernst}	Nernstian losses
δ	Thickness of the Stern layer
$\Delta\phi_{SC}$	Overpotential of the photocurrent
ϵ	Relative permittivity
ϵ_0	Permittivity of vacuum
ϵ_δ	Relative permittivity of the Stern layer
ϵ_r	Relative permittivity of water
ϵ_{min}	Relative permittivity of confined water
η	Overpotential of the reaction
Γ	Surface excess
γ	Surface tension
$\gamma_\pm$	Activity coefficient of the electrolyte
κ	Inverse of the Debye length
λ	Wave length
$\mathbf{E}$	Electric field
$\mathbf{u}$	Convective flux velocity
ω_Σ	Average of the partial molar area of all components (for one surfactant it is the molar area of the surfactant)
Φ	Quantum yield
$\phi(\lambda, x)$	Photon flux at a distance x in the beam direction
$\phi_0(\lambda)$	Photon flux
π	Surface pressure
ρ	Number density
ρ_e	Electric charge density
σ	Surface charge
σ_e	Contact free energy per unit area
τ	Half-life time of the photocatalyst's excited state
θ	Surface coverage of the catalyst with the reactant
θ_i	Surface coverage of the surfactant i
a_e	Area of the surfactant head
a_G	Fitting parameter
a_i	Activity of the species i
b	Adsorption constant
c_R^*	Concentration of excited reactive sites
c_0	Bulk concentration of species
C_i	Concentration of the charge carrier i
c_i	Bulk concentration of the species i
c_R	Concentration of unexcited reactive sites
$c_{ox,bulk}$	Bulk concentration of species involved in the anodic reaction
$c_{ox,surf}$	Surface concentration of species involved in the anodic reaction
$c_{R,0}$	Concentration of the total reactive sites
$c_{red,bulk}$	Bulk concentration of species involved in the cathodic reaction
$c_{red,surf}$	Surface concentration of species involved in the cathodic reaction
D_i	Diffusion coefficient of the species i
d_i	Diamater of the solvated species i
e	Elementary charge
$E°$	Standard thermodynamic equilibrium potential
F	Faraday constant
f	Fugacity of the gas
f_G	Efficiency of gas evolution at the electrode
G	Generation rate of the charge carrier
j	Current density
j_0	Exchange current density
$j_{0,ox}$	Exchange current density at the anode
$j_{0,red}$	Exchange current density at the cathode
j_{dark}	Dark current density at the anode
j_{ox}	Current density at the anode
j_{photo}	Photocurrent density at the anode
j_{red}	Current density at the cathode
k	First order rate constant of the redox reaction on nanoparticles
k^*	Rate constant k normalized to the catalyst concentration
K_0	Henry's law constant
k_B	Boltzmann constant
k_r	Recombination forward rate constant
k_1	Forward reaction constant of the redox reaction on molecular photocatalyst
k_2	Forward reaction constant of the regeneration of the photocatalyst
K_{ads}	Adsorption constant of the Langmuir adsorption isotherm
k_{CO_2}	Forward reaction constant of CO_2 dissociation
$k_{HCO_3^-}$	Forward reaction constant of HCO_3^- dissociation
l_0	Length of the surfactant tail
L_p	Local volumetric rate of photon absorption
m	Coefficient equal to 1 for non-ionic surfactant or ionic surfactant with large excess of salt and equal to 2 for ionic surfactants
m_0	Mass concentration of the catalyst
M_{water}	Molar concentration of water
N	Number of moles of electrons
n	Number of electrons
N^+	Number of cations
N^-	Number of anions
n_0	Electron donor density in an n-type semiconductor
N_A	Avogadro number
N_D	Flux density of formation of the gas

electrochemical potential (−1.90 V vs Normal Hydrogen Electrode — NHE) [22]. Other proposed reaction mechanisms bypass the formation of the radical $CO_2^{-\cdot}$ by involving a series of multiple proton-coupled

N_G	Flux density of formation of the gas converted into bubbles
n_G	Fitting parameter
N_m	Aggregation number of monomers in a micelle
n_s	Number of species i in solution
P_a	Acceptance probability for the insertion move
P_d	Acceptance probability for the deletion move
P_t	Acceptance probability for the translation move
$p_{CO_2,bulk}$	Partial pressure of the CO_2 in the bulk
$p_{CO_2,c}$	Partial pressure of the CO_2 at the cathode
pH_a	pH at the anode
pH_c	pH at the cathode
pH_{bulk}	pH in the bulk
pK_1	pK value for the dissociation of CO_2
pK_2	pK value for the dissociation of HCO_3^-
q_i	Charge of the particle i
R	Universal gas constant
r	Reaction rate
R_i	Recombination rate
S_i	Source term related to chemical reactions
T	Temperature
U_{ij}	Interaction energy between the particles i and j
V	Electric potential
V_0	Electric potential at a charged interface
v_0	Volume of the surfactant tail
V_δ	Electric potential at the end of the Stern layer
V_l	Potential in the electrolyte
V_s	Potential at the electrode
Vol	Volume of the simulation box
w_i	Parameter related by the number of water molecules held by the ion i
x	Distance
y	Dimensionless potential electric potential
y_0	Dimensionless potential electric potential at distance zero from the charged surface
Z_i	Charge number

electron transfers (PCET) thus requiring less electrochemical potential [23,24]. CO_2 adsorption on a semiconductor surface is one method of activating the otherwise inactive molecule for reduction [22]. In general, the surface atoms of the photocatalyst coordinate with the carbon or the oxygen atoms of the CO_2 molecule as shown in Fig. 1. The different binding modes partly determine the reaction pathways [21]. Depending on the reaction pathway and the number of electron transferred, it is possible to obtain multiple different products such as carbon monoxide, formic acid, formaldehyde, methanol and methane [25]. Among many products obtainable from CO_2, CO is a gaseous compound that requires the transfer of only two electrons, and thus it is a kinetically favorable choice as compared for example to methane, which requires the transfer of eight electrons to form one molecule as shown in Table 1. Moreover, a mixture of CO and H_2, coming from the proton reduction of water, can be employed in chemical reactors to produce more complex hydrocarbons through the Fischer–Tropsch process [26,27]. The obtained energy rich fuels such as methanol or methane, can be already used in the current infrastructure [28–30]. In Table 1 electrochemical CO_2 reduction potentials versus the NHE are reported.

One of the main challenges in CO_2 reduction is the large excess of protons in water solutions that can be reduced in the place of CO_2 [31,32]. Indeed, proton reduction does not have a high redox

Table 1
Reaction potentials of some reduction and oxidation reactions of interest [22].

Reaction	E°_{redox} vs NHE [V]
$CO_2 + 2H^+ + 2e^- \longrightarrow HCOOH$	−0.61
$CO_2 + 2H^+ + 2e^- \longrightarrow CO + H_2O$	−0.53
$CO_2 + 4H^+ + 4e^- \longrightarrow HCHO + H_2O$	−0.48
$CO_2 + 6H^+ + 6e^- \longrightarrow CH_3OH + H_2O$	−0.38
$CO_2 + 8H^+ + 8e^- \longrightarrow CH_4 + 2H_2O$	−0.24
$2H^+ + 2e^- \longrightarrow H_2$	−0.41
$2H_2O + 4H^+ \longrightarrow O_2 + 4H^+$	0.82

potential and requires small overpotential since it is a double electron process (see Table 1) [33]. During the last decades, researchers have investigated different methods and strategies to make CO_2 reduction more efficient working on materials and electrode design [22,34–37].

The CO_2 reduction reaction is ideally coupled with an oxidation reaction which provides the necessary electrons (and protons) to create a closed loop. In this work, we will focus on the water oxidation reaction, which generates oxygen. However, water oxidation to oxygen is a four electron process thus requiring high overpotentials. So, other oxidation reactions have been studied in literature to lower the potential necessary to obtain the desired product deriving from the CO_2 reduction [18,38,39]. Glycerol oxidation is a rather common reaction coupled with carbon dioxide reduction [18] or proton reduction [39]. Coupling CO_2 reduction and water oxidation is particularly challenging, so many studies focus on one of the two half-reactions, the reduction or the oxidation, achieved involving sacrificial electron donors or acceptors.

There are multiple possible approaches to generate solar fuels [40,41] as schematically depicted in Fig. 2:

- photocatalysis in solution
- photoelectrocatalysis in photoelectrochemical cells (PEC)
- thermochemical conversion of carbon dioxide and water to fuels at high temperature powered by concentrated solar light
- biomass conversion
- electrocatalysis by using the electricity generated in a photovoltaic panel to run an electrolyzer

While electrocatalysis and biomass gasification are examples of indirect methods for solar fuel production, where an additional step between the solar energy absorption and the generation of the fuel is added, the remaining approaches can be categorized as direct methods for the production of fuels.

There are still some key challenges for producing solar fuels on an industrial scale through photocatalysis, which, focusing on the technological aspects, can be divided in designing better materials and optimizing photochemical reactors. Developing highly efficient and stable photocatalysts is a major challenge since many photocatalysts exhibit limited efficiency and undergo degradation and deactivation over time [50]. Many photocatalysts have been designed inspired by natural photosynthesis. Those can be based on semiconductors [51,52] or molecular structures [53]. Hybrid systems are also common where semiconductors are decorated with noble metals or with other semiconductors [54–58], molecular catalysts [59,60], enzymes [61,62] or bacteria [63–65] in order to improve their efficiency and selectivity or to produce more complex molecules (e.g. multi-carbon compounds). For example, in [56], TiO_2 N-doped graphene catalysts decorated with Au nanoparticles have been synthesized and tested for CO_2 photo reduction to fuel using visible light with a high selectivity and efficiency towards methane. Thanks to both theoretical calculations and experimental testing, Authors identified the causes in the more favorable kinetics due to the N-graphene doping and to the extended visible light absorption and improved charge separation due to the Au nanoparticles. Likewise, molecular catalysts can be attached to semiconductors to improve their performances. In Ref. [59], ZnSe quantum

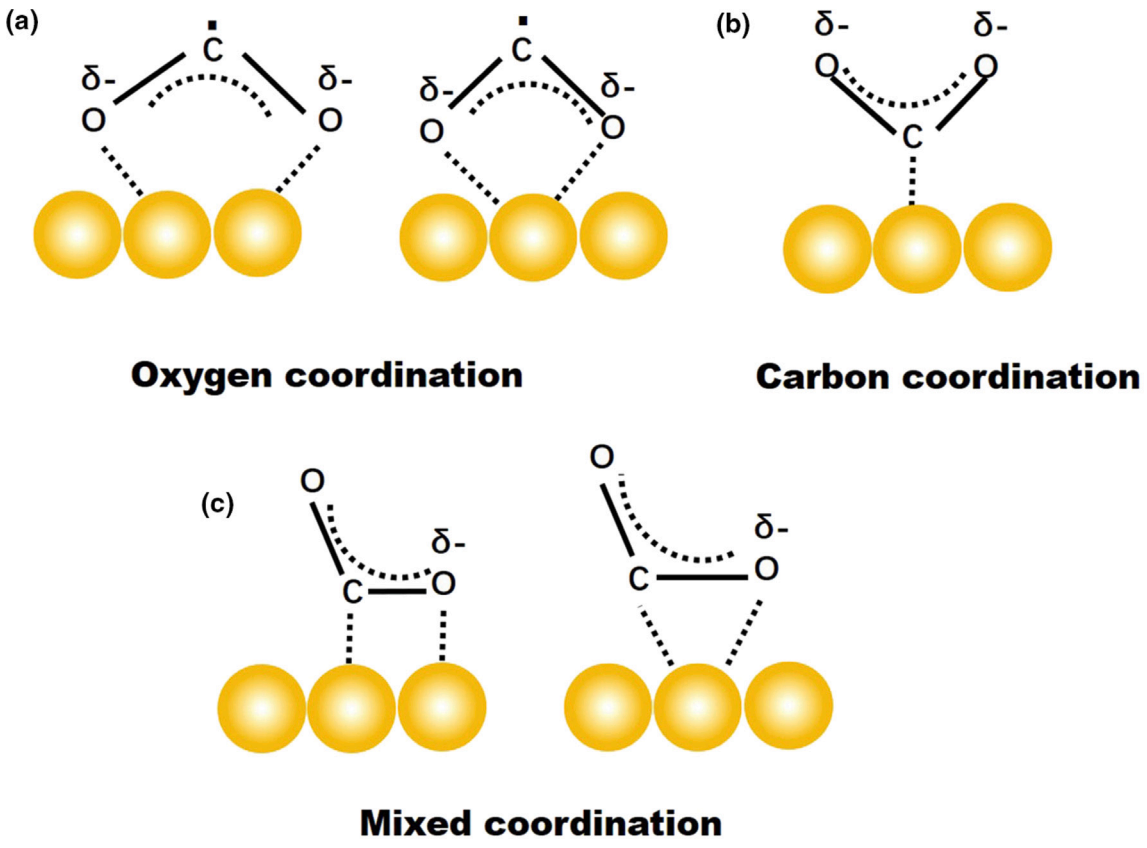

Fig. 1. Examples of CO_2 adsorption on the surface of a photocatalyst. The CO_2 molecule does not have a dipole moment, however each oxygen atom have a pair of electrons that can be donated to the adsorption sites on the surface (a). On the other hand, electrons from the adsorption site can be accepted by the carbon atom (b). Mixed coordination can occur when the CO_2 molecule act as an electron donor and acceptor (c).
Source: From [21].

dots were modified with the addition of a nickel based molecular catalyst, which resulted in a threefold increase of CO production due to better kinetics. Enzymes can be attached to nanoparticles [61] or porous electrodes to lower the kinetic barrier for CO_2 reduction and improve the selectivity [66]. Kuk and coworkers [66] designed a tandem photoelectrochemical cell where the reduction of CO_2 to formate was successfully reached thanks to a cathode where enzymes are attached to an electrically conductive titanium nitride structure. The electrons were provided by a bismuth vanadate photo anode for water oxidation and a perovskite photovoltaic cell used to produce the necessary potential for the CO_2 reduction. Similarly, bacteria can be used coupled with photoactive materials. In [67], CdS nanoparticles have been used as light absorbing units which deliver electrons to the attached non-phototrophic bacteria for CO_2 to CH_4 conversion.

Another challenge for up-scaling solar fuel production through photocatalysis lies in the reactor design and optimization towards a uniform illumination [68] and an efficient mass transfer. In this regard, monolith reactors with honeycomb structure holding photoactive nanoparticles have been investigated because of their potentially high surface to volume ratio and easily controllable of structural parameters (i.e., pore volume, pore size and surface area) [36]. Other researchers are focusing on gas diffusion electrodes for photoelectrochemical cells in order to improve mass transfer especially when dealing with gaseous species thus avoiding solubility issues [69].

1.1. Photocatalysis in solution

A possible reactor design involves the use of particles or molecular photocatalysts in gas phase or dissolved in solution. In this type of devices, charge carriers are generated by solar irradiation in each unit (e.g. a particle) which catalyses one of (or both) the half-reactions for fuel production and water oxidation. The case of proton reduction to hydrogen on a photoactive nanoparticle is shown in Fig. 2A. As it will be shown in the next sections, a photocatalytic process can be divided in different phases starting from the semiconductor (or molecule) which absorbs photons and generates excited electrons and holes (light harvesting). Successively, the separated charge carriers will drive the oxidation reaction (for example water oxidation to oxygen) and the reduction reaction (e.g., proton reduction to molecular hydrogen). The electrons and holes may recombine inside the bulk and the surface of the photocatalyst. We can distinguish these reactors in two types: Type 1 reactors in which the colloidal suspension is in a single vessel where both fuel production and oxygen evolution reaction occur and Type 2 reactors that consists of two different vessels (one for the fuel evolution and the other for the water oxidation) separated by a membrane. Type 1 reactors do not need wiring and have simple and low-cost photocatalytic reactor design. However, the oxygen and the gaseous fuel evolving in the same vessel might generate an explosive mixture and need to be separated afterwards. The reactor reported in [70] is an example of Type 1 rector, where a gaseous mixture of water and CO_2 reacts on titania nanoparticles doped with Iridium to produce a mixture of methane, ethane, ethene, propene, carbon monoxide and oxygen. Authors also compared two reactor designs, the first one involving a monolith coated with nanoparticles and the second one where the nanoparticles were suspended. The yield of CO per gram of catalyst resulted to be higher in the first case. In Type 2 reactors, the two half-reactions of water oxidation and fuel production generate intermediate chemical species that serve as a redox shuttle between the vessels via a Z-scheme mechanism [71]. This type of reactor has the advantage of separating the produced fuel from the generated oxygen, but present more technical challenges related to the redox shuttle flow. Indeed,

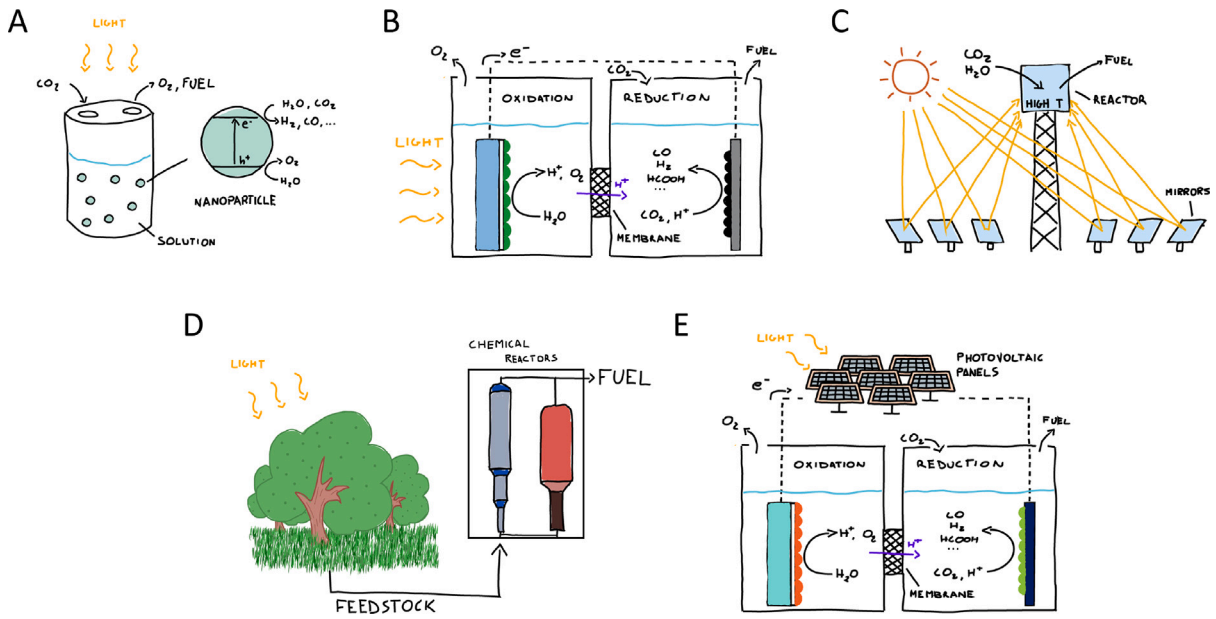

Fig. 2. Pictorial overview of different methods for solar fuel generation divided by reactor types. (A) Photocatalysis in a photochemical reactor where nanoparticles (or molecular structures) are responsible for the light harvesting and subsequent photoreactions. In the zoom, a nanoparticle with its valence and conduction bands is depicted, the photoexcited electrons (e^-) and holes (h^+) drive the reduction and oxidation reactions, respectively. (B) Photoelectrocatalysis in a PEC cell, the two compartments of water oxidation and fuel production are separated by an ion conductive membrane (inspired by [42]). In the picture, the anode is responsible for the photogeneration of the charge carriers and for the oxidation of water, while fuel production occurs at the cathode. Not all PEC cells adopt a membrane to separate the oxidation and reduction compartments [43]. (C) Thermochemical conversion through concentrated solar power (CSP), fuels are produced in a reactor at high temperatures (1000–2000 K) reached thanks to concentrated solar radiation using mirrors. At high temperatures, the CO_2 reduction path to fuels is thermodynamically favorable [44]. (D) Fuel production from biomass. This category include very different technologies such as thermochemical cycles involving combustion, gasification, pyrolysis, liquefaction, carbonization, or co-firing (depicted in the Figure) [45] or fermentation in reactors using bacteria [46]. (E) Water electrolysis and CO_2 reduction performed in electrolyzers powered by a photovoltaic (PV) power station [47,48]. A schematic view of an electrolyzer cell coupled with PV panels is reported. Note that electrolyzers are usually made of multiple cells stacked together [49].

most probably the redox shuttle will move in the reactor by mixing and diffusion. Simple diffusion without convection could reach a steady state profile in days depending on the size of the reactor. Thus, a slow redox-shuttle mass transport is one of the key factors, together with the kinetic of the two reactions (water oxidation and fuel evolution) and recombination issues, in determining the overall efficiency of the reactor.

Colloidal suspension can be made of:

- nanoparticles (e.g. based on metal oxides [35,71,72] or graphitic carbon nitrides [73,74])
- molecules (e.g. ruthenium based compounds [75], porphyrins [53] or enzymes for water oxidation [75] or CO_2 reduction [53, 61])

Mixed systems where molecular catalysts are anchored to nanoparticles [59] or enclosed in self-assembled structures are widely reported in the literature [76–78].

For the case of colloidal suspension based on semiconductor powder, the nanoparticles are usually responsible for the light-absorption while a catalyst is responsible for an efficient charge separation and reduces the overpotential required for the redox reaction. These catalysts can be active molecules anchored to the light absorbing nanoparticle or noble metal cocatalysts (i.e., Pt, Pd, Au, Ag) [79]. For more details, Ref. [71] offers an extensive analysis of visible-light-driven particles for water oxidation and proton reduction with and without cocatalyst, whereas the interested reader can find in [54] a thorough analysis on the different strategies to anchor molecular catalysts to a wide range of substrates such as carbon nanotubes, quantum dots, metal oxide surfaces, and semiconductors.

Molecular metal complexes made of metal ions/clusters and organic ligands are increasingly attracting attention in the field of photocatalysis for solar fuel production since their redox potential and light harvesting capability as well as their selectivity can be tuned by acting on their molecular structure [40,80,81]. This allows to obtain high products selectivity and quantum efficiencies. Molecular photocatalysis can be performed both by a single molecule which acts as light absorbing unit and catalyst [82] or by two or more molecules mimicking the natural photosynthesis process where photons are absorbed and collected by photosensitizers and then transferred from or to a second molecule responsible for the redox reaction, the catalyst [53,75]. An example of selective CO_2 reduction to CO in solution driven by a ruthenium tris(bipyridine) photosensitizer (PS) and a cobalt based soluble porphyrin catalyst (C) is reported in Ref. [53] and summarized in the pictorial representation of Fig. 3. Authors focused on the CO_2 half-reaction using sodium ascorbate as sacrificial electron donor (ED). This process can be divided in three steps:

- the reductive quenching of the excited state of the photosensitizer by the sodium ascorbate
- the electron transfer from the photosensitizer to the catalyst
- the catalytic reduction of CO_2 to CO

Authors found that the high selectivity to CO of the cobalt based porphyrin was caused by one of its reaction intermediates that is stabilized by the attached CO_2 molecule, thus reducing the probability of the formation of other intermediates which would have led to hydrogen evolution. In Ref. [53], a more accurate and quantitative description of the reaction mechanism of the CO_2 reduction to CO is given.

Among the various molecular photosensitizers [83,84], the same ruthenium showed before is widely used in literature also for water oxidation due to its high reductive and oxidative potential [85]. Authors in Ref. [75] compared a water oxidation to oxygen driven by two different ruthenium catalysts using sodium persulfate as sacrificial electron acceptor. As before, three major steps can be identified:

- the oxidative quenching of the excited state of the photosensitizer by the sodium persulfate
- the electron transfer from the catalyst to the photosensitizer

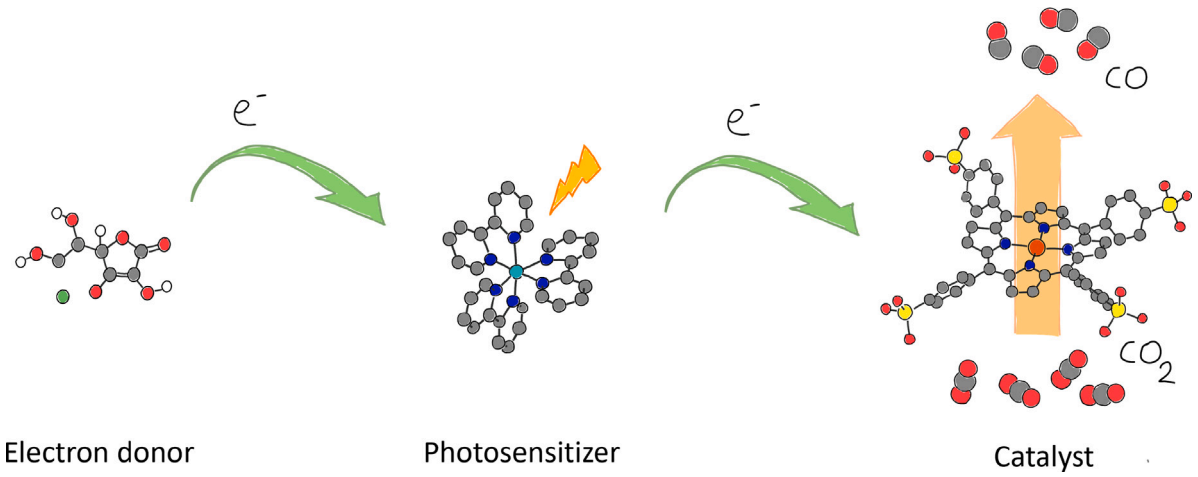

Fig. 3. Generic reaction steps for the reduction of CO_2 to fuel using molecular photosensitizers and catalysts: (1) light absorption by the photosensitizer, whose exited state is quenched by an electron donor; (2) multiple electron transfer from the photosensitizer to the catalyst which stores the electrons (two for the analyzed case) and 3) reduces CO_2 to CO. In this picture the electron donor, the photosensitizer and the catalyst are sodium ascorbate, ruthenium tris(bipyridine) and a cobalt based porphyrin, respectively [53].

- the catalytic oxidation of water to oxygen

One of the main challenges of those particulate/molecular photocatalysts system is the stability of their components. For this reason, many authors have investigated how to improve the stability and the efficiency of molecular catalysts and photosensitizers by enclosing them in supramolecular and self-assembled structures such as micelles [77,86,87] and liposomes [76,88]. Micelles are assemblies of amphiphilic molecules whose hydrophobic tails form an oil-like environment inside the aggregate while the hydrophilic head groups face the surrounding media. Similarly liposomes are vesicles, spherical in shape, having at least one lipid bilayer separating the inner part of the liposome from the solution. Catalysts and photosensitizers in supramolecular structures are closer to each other as compared to those within homogeneous solutions thus possibly leading to enhanced intermolecular interactions. This leads to more effective charge separation with less charge recombination as compared to the same compounds in homogeneous systems [89]. Moreover, self-assembled structures help to solubilize the photoactive molecules as well as protect them and their intermediates [87]. Wang and coworkers [82] solubilize an hydrophobic tin porphyrin in micelles to stabilize the molecule during water oxidation to oxygen. Self-assembled structures can be used to separate the two reactions of oxidation and reduction providing compartmentalization of the products [87].

Most of molecular-based systems under study focus on one reaction (oxidation or reduction) employing sacrificial agents due to some open issues related to different redox environments of the reduction and the oxidation, charge recombination, different solubilities of the products and their separation. In particular, oxygen may severely interfere with the photochemical reactions [87]. Self-assembled structures can help to solve part of these problems as demonstrated by the work of Hu and coworkers [90] who were able to compartmentalize in the same liposome two types of metal organic frameworks responsible for the water oxidation and hydrogen production half-reactions, respectively.

1.2. Photoelectrochemical cells (PEC)

In photoelectrochemical cells, the solar energy harvested by a semiconductor leads to the generation of charge carriers, namely electrons in the conduction band and holes in the valence band. While the electrons flow in an external circuit reaching the cathode for the reduction of protons or CO_2 to the desired fuel, the holes accumulate at the anode driving the water oxidation half-reaction. In 1972, Fujishima and Honda [51] published a seminal paper describing the photocatalytic properties of titanium dioxide, which was used to produce hydrogen and oxygen from water splitting. The configuration of the cell was similar to the one shown in Fig. 2B, with two electrodes immersed in an electrolyte and separated by a membrane. The latter served as separator to limit electrolyte and product crossover, thus increasing the performance of the cell [91]. Upon irradiation of the TiO_2 electrode surface, electrons flow from the TiO_2 to the platinum electrode via the external circuit. The direction of the electron flow reveals that the oxidation half-reaction (oxygen evolution) occurs at the TiO_2 electrode and reduction half-reaction (hydrogen evolution) at the platinum electrode. We can divide the solar-to-fuel (hydrogen for the case of Fujishima) process in three steps as reported in Table 2.

Table 2
Steps in the photocatalytic splitting of water in the PEC reported in [51].

(1) Light harvesting and charge separation	$TiO_2 + 4h\nu \longrightarrow 4e^- + 4p^+$
(2) Water oxidation (at the TiO_2 electrode)	$4p^+ + 2H_2O \longrightarrow O_2 + 4H^+$
(3) Proton reduction (at the platinum electrode)	$4e^- + 4H^+ \longrightarrow 2H_2$
Overall reaction	$2H_2O + 4h\nu \longrightarrow O_2 + 2H_2$

Since then, PECs have been investigated not only for proton, but also, for CO_2 reduction. More sophisticated electrodes and devices are necessary in order to reduce efficiently and selectively CO_2 in water as in aqueous media the hydrogen evolution reaction also takes place and can be driven by a lower overpotential than the one necessary for CO_2 reduction. Indeed, selectivity depends on many factors such as the catalyst material, morphology, surface modification and reaction conditions. Those aspects have a direct influence on the different characteristics of the photo electrodes such as the adsorption/desorption of intermediates, adsorption of the reactants, light-excitation, band structure and separation of photogenerated charge carriers [21]. For example, Iizuka and coworkers [92] studied the effect of the cocatalyst in the CO_2 Reduction over $ALa_4Ti_4O_{15}$ (A = Ca, Sr, and Ba) photocatalysts: Authors discovered that Ag could be a good cocatalyst for photocatalytic CO_2 reduction due to non-favorable surface for proton reduction and that, while the bare $BaLa_4Ti_4O_{15}$ produced only hydrogen, the addition of a silver cocatalyst resulted in a change of the product selectivity towards CO. Chu and coworkers [26] demonstrated an efficient photoelectrochemical CO_2 reduction for syngas production with a controlled H_2/CO_2 mixture composition by employing a metal/oxide nanostructured interface. Other researchers [60] included a molecular catalyst on the semiconductor electrode in order to improve selectivity and efficiency of the PEC cell. A wireless configuration of the PEC cell has been also studied in literature where both the oxidation reaction and the reduction reaction occur on the same artificial leaf [42].

Table 3
Main categories of models for describing chemical phenomena in photo(electro)chemical devices.

Model category	General description	Advantages and main use	Disadvantages	Main ref.
Kinetic models	These types of models consist of a system of equations describing the different reaction steps (light absorption, redox reaction steps) and intermediates with variable accuracy. In the case of multiple reaction steps and pathways, these models are defined as micro-kinetic models, sometimes coupled with ab initio simulations for calculating a priori the reaction constants.	• Describing and optimizing the reaction mechanisms finding possible rate determining steps for photochemistry in solution (nanoparticles or molecular catalysts). • Fast computation.	• Do not consider mass transport. • In the case of complex reaction mechanisms, a large number of simulations and/or experiments are required.	[93–95]
Macroscale continuum models	Multiphysics macroscale models consist of a system of equations coupling the reactive part (kinetic model) and mass transport (diffusion and convection) solved in a specific domain which can be 1D, 2D or 3D.	• Considering the competition between the different phenomena such as: mass transport, light absorption, charge carriers diffusion, charge effects such as the electric double layer, chemical reactions, bubble formation and fluid flow. • Studying and optimizing chemical reactors such as photoelectrochemical cells.	• The nanoscopic structure of the matter is usually taken into account by effective parameters. • High computational cost for complex computational domains.	[33,96,97]

2. Chemical phenomena: models for reactive interfaces

A fundamental understanding of the phenomena occurring during the photocatalytic reactions is essential for the optimization of future devices for solar fuel production. A detailed reaction kinetics coupled with mass-transport phenomena is indeed necessary for designing more effective interfaces achieving remarkable performance gains [98]. In this section, we focus on continuum models, mesoscale models, atomistic simulations and kinetic models in a coherent multiscale perspective as summarized in Table 3. Detailed reaction pathways investigated through *ab initio* simulations and density functional theory (DFT) are out of the scope of this work, although they are crucial tools for studying photo(electro)chemical reactions [99–101]. *Ab initio* simulations are especially helpful when integrated with experimental techniques to identify critical reaction intermediates and rate determining steps building a microkinetic model of the reaction mechanism under study [102–104]. However, the number of parameters to consider in photocatalytic experiments to build an accurate microkinetic model rapidly increases. Thus, many researchers are focusing their effort in coupling experimental and modeling techniques with machine learning algorithms to foster the discover of new mechanisms and to optimize the experimental conditions [105–107]. In the following sections, we first focus on general kinetic models for systems made of colloidal suspensions and, subsequently, on continuum models of reactive interfaces.

2.1. Homogeneous systems

Bloh and coworkers [93] developed a kinetic model for photoreactions on nanoparticles and molecules as shown in Fig. 2A. Authors focused on the slower and rate determining half-reaction and divided the process in three reaction steps as shown in Fig. 4A. The first one is the generation of a reactive site c_R^*, that corresponds to a surface site in which an electron (or a hole) is trapped and thus capable to reduce (or oxidize) a reactant (e.g. CO_2) generating the desired product (e.g. CO). The rate of this reaction step was defined as:

$$r_1(c_R \longrightarrow c_R^*) = \boldsymbol{\Phi} \cdot L_p \cdot \frac{c_R}{c_{R,0}} \tag{1}$$

where L_p is the local volumetric rate of photon absorption, $\boldsymbol{\Phi}$ is the quantum yield, c_R^*, the concentration of excited reactive sites, c_R the concentration of unexcited reactive sites and $c_{R,0}$ the concentration of the total reactive sites. The quantum yield takes into account all the losses (e.g. bulk charge recombination). The surface charge recombination with a reactive site that relaxes to its ground state was considered as a first order reaction by adding a second reactive step:

$$r_2(c_R^* \longrightarrow c_R) = k_r \frac{c_R^*}{c_{R,0}} \tag{2}$$

with k_r being the recombination rate constant. The final step is the redox reaction of adsorbed reactant S in the active site:

$$r_3(c_R^* + S \longrightarrow c_R + P) = k \cdot \theta \cdot c_R^* \tag{3}$$

$$\theta = \frac{K_{ads} \cdot [S]}{1 + K_{ads} \cdot [S]} \tag{4}$$

where P are the products of the chemical reactions. A Langmuir adsorption isotherm, Eq. (4), was employed for the adsorption of reactants with concentration S and adsorption constant K_{ads}. θ is the surface coverage of the photocatalyst. It is possible to define the overall reaction rate by assuming a pseudo-steady-state approach ($c_R, c_R^* = const.$, $r_1 = r_2 + r_3$). Normalizing the rate constant to mass concentration of the catalyst m_0, the rate r can be defined as:

$$r = \frac{\boldsymbol{\Phi} \cdot L_p \cdot k^* \cdot \theta \cdot m_0}{\boldsymbol{\Phi} \cdot L_p + k_r + k^* \cdot \theta \cdot c_0} \tag{5}$$

$$k^* = \frac{k \cdot c_{R,0}}{m_0} \tag{6}$$

In Eq. (5), θ can be obtained from Eq. (4) while L_p can be estimated by using the Lambert–Beer law for calculating the light absorption of the solution, for a non monochromatic light:

$$\phi(\lambda, x) = \phi_0(\lambda)\, e^{-\alpha(\lambda)x} \tag{7}$$

$$L_p(x) = -\int_{\lambda_{min}}^{\lambda_{max}} \frac{d\phi(\lambda, x)}{dx} d\lambda = -\int_{\lambda_{min}}^{\lambda_{max}} \alpha(\lambda)\phi_0(\lambda)\, e^{-\alpha(\lambda)x} d\lambda \tag{8}$$

with ϕ_0 being the photon flux, $\alpha(\lambda)$ the absorption coefficient of the solution and x the propagation direction of the photon flux. The three remaining parameters, namely the rate constant (k^*), the quantum yield ($\boldsymbol{\Phi}$) and the recombination rate (k_r), can be found by best-fitting the model to experimental data. Eq. (5) shows that for low light intensity, the reaction is dominated by the flux of absorbed photons. On the other hand, for high light intensities the rate is limited by the reaction kinetics. The above theoretical framework was applied by Bloh

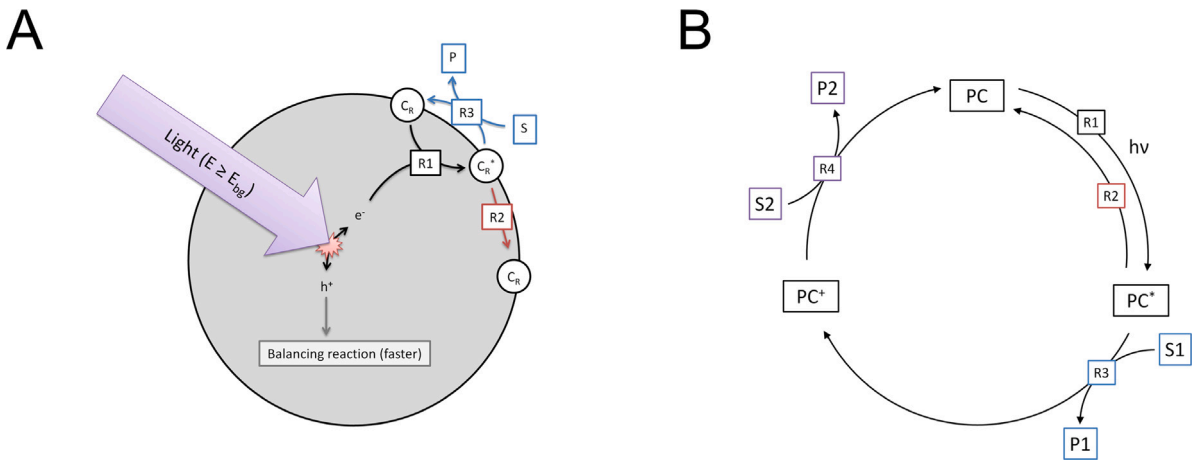

Fig. 4. Kinetic models for a generic photoreaction. (A) kinetic model for a generic photoreaction on a nanoparticle. In the first step (R1), if the incoming photons have an energy ($h\nu$) higher than the band gap of the semiconductor (E_{bg}), than the excited state is generated (c_R^*). R2 considers charge recombination thus the relaxation of the excited state to its ground state (c_R). R3 represents the charge transfer and the chemical reaction, being S and P in the Figure the reactants and the products, respectively. (B) Four steps considered in the model for a molecular photocatalytic reaction occurring on a photocatalyst (PC). Once the excited state is reached (R1), the molecule can relax (R2) or undergo an oxidative (or reductive) quenching (R3). Finally, the photocatalyst is regenerated (R4).
Source: From [93].

and coworkers [108] for describing and optimizing the photocatalytic reduction of nitrobenzene to aniline in alcoholic solutions using titania nanoparticles. Authors studied the effect of light intensity, catalyst concentration, initial concentration and temperature to eventually optimize the reaction conditions. It is important to note that the Equations presented so far depends on the local photon flux that might vary in the reaction medium, for example due to scattering, adsorption or reflection [109]. However, it is still possible to assume the average photon flux to calculate the reaction rate if the reaction rate depends linearly on the light intensity. This theoretical framework has some drawbacks related to its simplicity. For example, dynamic processes cannot be modeled due to the steady state assumption. Moreover, the model does not consider changes in the solution properties, such as pH, and the depletion of the photoactive species. Finally, this simplified model does not take into account mass transport in solution and do not consider concerted multi-electron transfers.

More tailored descriptions of the reaction mechanisms of solar fuel production through photocatalysis have been developed. For example, Bjelajac and coworkers [94] adopted a microkinetic model to describe the CO_2 reduction reaction on titania nanoparticles for the generation of hydrogen, methane and carbon monoxide in a monolith reactor. Authors compared the performances of four photocatalysts by using experimental data to best-fit the microkinetic model of photocatalytic production of CH_4, CO and H_2 from a gas mixture of CO_2 and water. Four surface reactions on the nanoparticle and six adsorption/desorption reactions of the reactants and the products were considered:

$$CO_{2(g)} + 1^* \rightleftharpoons CO_2^* \tag{9}$$

$$H_2O_{(g)} + 1^* \rightleftharpoons H_2O^* \tag{10}$$

$$2H_2O^* + 3^* \longrightarrow 4H^* + O_2 * \tag{11}$$

$$2H^* \longrightarrow H_2^* + 1^* \tag{12}$$

$$CO_2^* + 2H^* \longrightarrow CO^* + H_2O^* + 1^* \tag{13}$$

$$CO_2^* + 8H^* \longrightarrow CH_4^* + 2H_2O^* + 6^* \tag{14}$$

$$CO_{(g)} + 1^* \rightleftharpoons CO^* \tag{15}$$

$$O_{2(g)} + 1^* \rightleftharpoons O_2^* \tag{16}$$

$$H_{2(g)} + 1^* \rightleftharpoons H_2^* \tag{17}$$

$$CH_{4(g)} + 1^* \rightleftharpoons CH_4^* \tag{18}$$

The star used as superscript in the Reactions (9)–(18) denotes the adsorbed state. When the star is used as a superscript of a number, this indicates how many active sites have been occupied or freed by the reaction. For example, for the case of CO_2 adsorption in Eq. (9), one surface site (1^*) will be occupied by the incoming molecule. This highlights the possible competition of the chemical species for the same reactive site and its effect on the final products. Indeed, Authors pointed out how the initial CO_2/H_2O mixture composition needs to be optimized to avoid excessively high H_2O concentrations which, by covering the catalyst active sites, would reduce the surface contact of CO_2 molecules with the photocatalyst. This is demonstrated by Authors in [110] who measured the adsorption isotherms and the heat of adsorption of water and carbon dioxide on titania suggesting that adsorption of water is stronger and with higher coverage than that of CO_2. Reactions (9)–(18) resulted in seven differential equations, one for each chemical species of interest (CO_2, H_2O, O_2, H_2, CO, CH_4), in addition to an equation describing the time evolution of the reactive sites. Initially, a total of 17 free parameters were considered, which was reduced to 4 by assuming fixed adsorption and desorption constants. Bjelajac and coworkers [94] found the four free parameters by fitting their experimental results. Authors were able to establish that the water dissociation to H radical and O_2 is the rate determining step of the reaction, while the formation of CO and CH_4 are the fastest reaction steps. Similar kinetic models for CO_2 reduction have been proposed for titania based nanoparticles [70,95,97].

An analogous approach, summarized in Fig. 4B, can be applied to homogeneous catalysis once Eqs. (1)–(3) are properly rewritten. Considering a photocatalyst which absorbs light and catalyses the reaction, in the first step, the photocatalyst (PC) is excited owing to the absorbed light. This can be related to the local volumetric rate of photon adsorption as in Eqs. (1):

$$r_1(PC \longrightarrow PC^*) = \Phi \cdot L_p \cdot \frac{[PC]}{[PC_0]} \tag{19}$$

with $[PC]$ being the concentration of the photocatalyst in the ground state, $[PC_0]$ the total concentration of photocatalyst and Φ the quantum yield of the reaction. Once the photocatalyst is in an excited state, it can relax back to the ground state (r_2) or undergo a reductive (or oxidative) quenching (r_3). For the first case, Bloh and coworkers [93] assumed a first order reaction with respect to the concentration of the excited state:

$$r_2(PC^* \longrightarrow PC) = \frac{[PC^*]}{\tau} \tag{20}$$

By assuming an identical behavior for the oxidative or the reductive quenching, Authors analyzed only the oxidative quenching:

$$r_3(PC^* + S_1 \longrightarrow PC^+ + P_1) = k_1 \cdot [S_1] \cdot [PC^*] \tag{21}$$

where S_1 is the reactant, P_1 the product and k_1 the rate constant. In the last step the oxidized photocatalyst (PS^+) is regenerated to the ground state (PC):

$$r_4(PC^+ + S_2 \longrightarrow PC + P_2) = k_2 \cdot [S_2] \cdot [PC^+] \tag{22}$$

being k_2 the rate constant of the second-order reaction, $[S_2]$ the concentration of the reactant and P_2 the product. A similar yet more complex 0-dimensional kinetic model was adopted by Limburg and coworkers [111] to describe photocatalytic reduction of methyl viologen by cysteine photoinduced by a tetraanionic zinc porphyrin in homogeneous conditions and in liposomes. Authors were able to demonstrate that the same molecules behave differently depending whether they find themselves in homogeneous systems or in liposomes structures. In particular, the kinetics of elementary steps changed dramatically with the rate of oxidative quenching of the electron acceptor (methyl viologen) increasing of two order of magnitudes due to the positively charged surface of the liposome and subsequent increase of products formation.

2.2. Photoelectrochemical (PEC) cells

In this section, we describe commonly reported strategies to model photoelectrochemical devices. Light absorption, charge transport, interfacial reactions and transport of (charged) species in solution all take place in PEC cells. Those phenomena occur at different time and length scales ranging from nanoseconds (and nanometers) of the electron transfer at the reactive interfaces up to minutes (and centimeters) of diffusion and convection mechanism of species in solution [112].

In the following, we summarize the main steps occurring during photoelectrocatalytic fuel production. Starting from the light absorption, assuming planar and nonporous semiconductor electrodes, we can estimate the local light absorption rate L_p using the above mentioned Beer–Lambert law (Eqs. (7) and (8)), where $\alpha(\lambda)$ is the absorption coefficient of the light absorber. For the case of multi-layer electrodes, more sophisticated models have been developed [113,114]. After light absorption, the charge carriers (electrons in the conduction band and holes in the valence band of the semiconductor) are transported to the interface where chemical reactions occur. The separation of the charge carriers in an electrode is usually due to the electric field developed at the interfaces of the different materials of the electrode itself [115]. The transport of electrons and holes in the semiconductor can be effectively described by a drift diffusion model [33]:

$$\frac{\partial C_i}{\partial t} = \nabla \cdot \mathbf{J}_i + G_i - R_i \tag{23}$$

where C_i is the concentration of the charge carriers (electrons or holes), G_i the generation rate of charge carriers, R_i the recombination rate and J_i the net flux defined as:

$$\mathbf{J}_i = -D_i \nabla C_i + \frac{D_i Z_i F C_i}{RT}\mathbf{E} \tag{24}$$

with Z_i being the charge number, $\mathbf{E}$ the electric field, D_i the diffusion coefficient, F the Faraday constant equal to $N_A e$, N_A the Avogadro number and e the elementary charge. The recombination rate R_i in Eq. (23) refers to the various recombination processes, such as radiative and nonradiative recombination. When an electron and a hole recombine, the released energy is absorbed by other particles. In radiative recombination, a hole reacts with an electron to produce a photon. It can be regarded as an electron in the conduction band transitioning spontaneously to an unoccupied state in the valence band. Nonradiative recombination processes can be divided in Auger recombination or impurity recombination. In the first case, the energy released by the recombination of an electron–hole pair is absorbed by a free carrier and dissipated through the generation of phonons in collisions with the lattice. In the second case, recombination occurs through traps in the forbidden gap of the semiconductor generated by impurities or defects in the lattice. These defects capture electrons and holes over a series of excited states, with successive dissipation of energy [116]. The electrons and the holes that reach the electrode surface drive one of the two half-reactions of fuel production or water oxidation.

The kinetics of interfacial reactions occurring at the electrode depend on many factors such the overpotential (defined as the difference between the thermodynamic potential and the electrode potential measured experimentally [117]) and the concentration of the reactants. For example, the overpotential required by redox reaction which involve few electrons (such as the hydrogen evolution) is smaller than those where multiple electron transfers are needed (e.g. the water oxidation). The Butler-Volmer relates the electrical current flowing through an electrode to the overpotential, η [118]:

$$j = j_0 \left(\left(\frac{c_{ox,surf}}{c_{ox,bulk}} \right) e^{\frac{\alpha_a n F \eta}{RT}} - \left(\frac{c_{red,surf}}{c_{red,bulk}} \right) e^{\frac{-\alpha_c n F \eta}{RT}} \right) \tag{25}$$

where j_0 is the exchange current density, α_a and α_c are the charge transfer coefficient of the anodic and cathodic reactions, a measure of the symmetry of the energy barrier of the reaction and in the case of absence of more specific experimental data can be assumed to be 0.5 [117]. T is the temperature and n the number of electrons. $c_{ox,surf}$, $c_{red,surf}$, $c_{ox,bulk}$ and $c_{red,bulk}$ are the surface and bulk concentration of species involved in anodic and cathodic reactions, respectively [117]. The exchange current density accounts for the charge transfer rate at the electrode/electrolyte interface at the equilibrium and it is calculated in the absence of a current flow: j_0 might vary from a few nanoamperes per square centimeter to a few amperes per square centimeter [119].

Hankin and coworkers [121] employed a continuum model to optimize the design of photoelectrochemical reactors. The simulated 3D domain of the PEC cell is shown in Fig. 5. Authors used the Nernst–Planck equation to describe the transport of charges in the electrolyte solution (reported in Section 3) and assumed the linearized Butler-Volmer equation (less computational expensive than Eq. (25)) to describe the current density behavior at the cathode:

$$j_{red} = j_{0,red} \left(\frac{nF\eta}{RT} \right) \tag{26}$$

The overall anodic current density was calculated as the sum of the photocurrent j_{photo} and of the dark current j_{dark} densities:

$$j_{ox} = j_{photo} + j_{dark} \tag{27}$$

where j_{photo} is generated owing to the incoming light irradiation and j_{dark} is due to the random generation of electrons within the depletion region of the device [122]. The photocurrent was modeled by the Gartner-Butler equation, which correlates the generated current density to the incident light irradiation:

$$j_{photo} \approx \left(\frac{2e(\sum_\lambda \phi_0(\lambda) \cdot \alpha(\lambda))^2 \epsilon \epsilon_0}{n_0} \right)^{1/2} (\Delta\phi_{SC})^{1/2} \tag{28}$$

where e is the elementary charge, n_0 the electron donor density in an n-type semiconductor, $\Delta\phi_{SC}$ the overpotential for the photocurrent defined as difference between the applied potential and the flat band potential, whereas $\alpha(\lambda)$ represents the adsorption coefficient of the

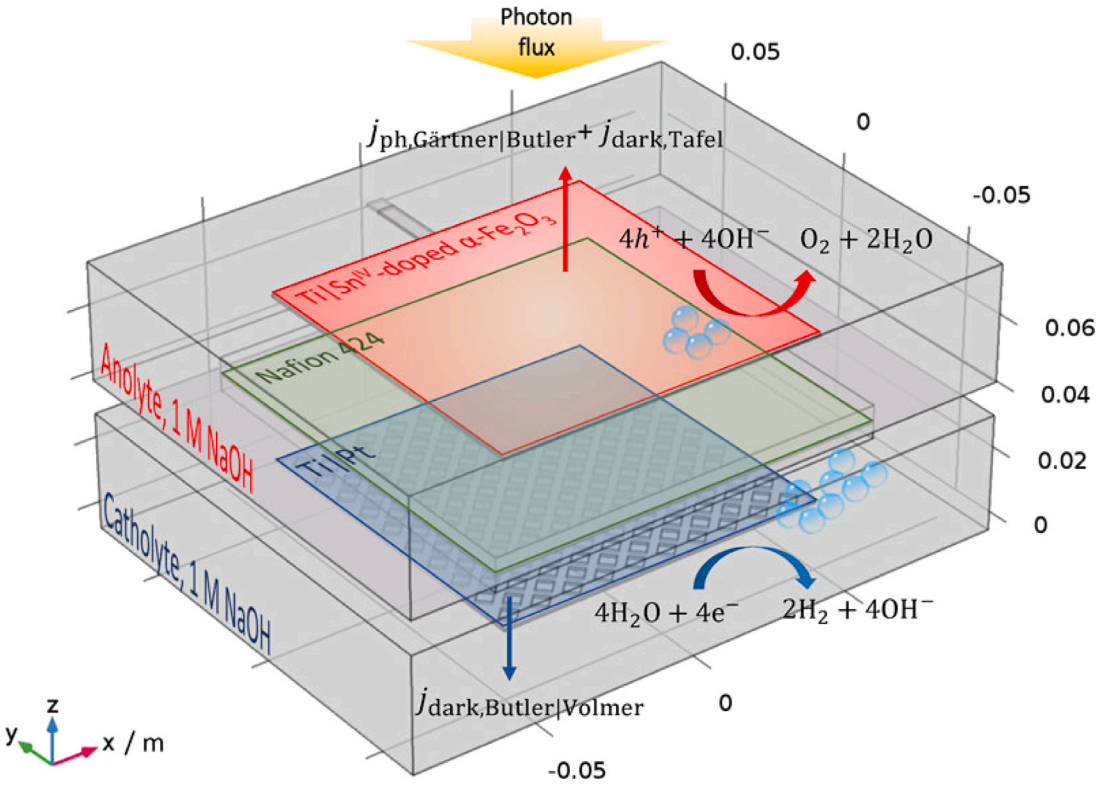

Fig. 5. View of the PEC cell showing the kinetic model applied at the electrode-solution interfaces. In particular, Eq. (27) is set as boundary condition at the anode (depicted in red), which is exposed to light and where oxygen evolves. The photoanode is 0.1×0.1 m^2. The dark cathode, where hydrogen evolution takes place, is highlighted in blue and the current density is described by Eq. (26). The ion permeable membrane which separates the produced hydrogen and oxygen is green colored. Both compartments are filled with 1 M NaOH (pH 13.6). The electrolyte is modeled as a homogeneous continuous medium.
Source: From [120].

semiconductor. Authors added a few corrections to Eq. (28) in order to take into account electron–hole recombination and the attenuation of the photon flux due to the quartz window, and the photon absorption by the thin film semiconductor. For the latter, the Beer–Lambert law was employed (see Eq. (7)). The Tafel equation, the approximation of the Butler-Volmer equation for large overpotentials [123], was used to describe the dark anodic current as [124]:

$$j_{dark} = j_{0,ox} e^{\beta\eta} \tag{29}$$

being $j_{0,ox}$ and η the exchange current density and the overpotential for the oxygen evolution reaction and $\beta = \alpha_a F/RT$ the Tafel coefficient. Bui et al. partially generalized Eq. (29) to take into account the effect of the local pH and the local reactant concentration [125], so that the micro environment at the electrode interface is considered. By applying the above mentioned model, Hankin and coworkers [121] were able to understand the effect of electrode geometries and configurations on photo-electrochemical reactors and evaluate the spatial distributions of potential, photon flux, and current densities. Moreover, they were able to describe the oxygen evolution photocurrent thanks to a micro-kinetic model based on experimentally determined parameters (semiconductor film thickness, band gap, absorption coefficient, relative permittivity, charge carrier density, flat band potential and electron–hole recombination efficiencies). The decrease of electrolyte conductivities and increasing activities of photo-anodes was found to cause greater inhomogeneities in the current density distributions. Possible alternatives depending on the materials under study and on the requested degree of detail are also available in literature to describe the photoexcitation process in the electrodes [33,126,127]. Other continuum models for electrochemical porous electrodes have been also studied and thoroughly investigated in [128].

Gas bubble formation at the electrodes has an effect on the reactions since reduces the available electrode area for the reactants and affects the radiation path through scattering [129]. A relatively simple model to consider this process was presented in [121] in which the bubble formation rates at the electrodes are related to the current density [130]:

$$\frac{f_G}{1 + f_G} = a_G j^{n_G} \tag{30}$$

where a_G and n_G are fitted from experimental data. f_G is defined as the efficiency of gas evolution as [131]:

$$f_G = \frac{N_G}{N_D} \tag{31}$$

where N_D is the flux density of formation of dissolved gas and N_G is the fraction of N_D converted into bubbles at the electrode surface. Eq. (30) have been validated for the case of hydrogen and oxygen bubbles generated at the nickel and platinum-wire electrodes in alkaline solution for current density between 10 to 10^4 A m^{-2}[132]. This approximate model does not take into account the two-phase flow due to bubble detachment [133,134]. Other models including the fluid flow phenomena described by the Navier–Stokes equations have been also developed for device optimization [97,135–137].

A detailed multiscale framework considering a continuum model for the transport of species coupled with a microkinetic model for the cathode reaction dynamics and DFT calculations for the estimate of the free energies of activation of the elementary reactions was proposed by Singh and coworkers [96]. Fig. 6 summarizes the proposed multiscale model. Referring to the continuum model, Authors adopted the Nernst–Planck equations for the transport of species in the electrolyte and in the membrane. The charge-transfer kinetics at the anode where the water oxidation is occurring, was modeled using the Tafel kinetics (Eq. (29)) with the overpotential of the catalyst given by:

$$\eta = V_s - V_l - E^\circ + \Delta V_{Nernst} \tag{32}$$

Here, V_s and V_l are the electrode and the electrolyte potential, whereas $E°$ is the equilibrium potential of the half-reaction at standard conditions. In the case of the water oxidation:

$$H_2O \longrightarrow \frac{1}{2}O_2 + 2H^+ + 2e^-, \quad E° = 1.229V \tag{33}$$

The Nernstian loss ΔV_{Nernst} was calculated as the sum of the difference in concentration of the CO_2 at the cathode with respect to the electrolyte, and the difference in pH at the two electrodes:

$$\Delta V_{Nernst} = \frac{RT}{NF} ln\left(\frac{p_{CO_2,bulk}}{p_{CO_2,c}}\right) + \frac{2.303RT}{F}(pH_c - pH_{bulk}) + \frac{2.303RT}{F}(pH_a - pH_{bulk}) \tag{34}$$

where N is the number of moles of electrons transferred per mole of CO_2, and p_{CO_2} the partial pressure of CO_2. The kinetics of the CO_2 and proton reduction was accurately described by the microkinetic model coupled with DFT simulations showed in Fig. 6. Moreover, Authors assumed equilibrium reactions for the CO_2 dissolved in water. The equilibrium CO_2 between the gas and the liquid phase is given by the Henry Law:

$$K_0 = \frac{c_{CO_2}}{f_{CO_2}} \tag{35}$$

where c_{CO_2} is the concentration of the CO_2 dissolved in water and f_{CO_2} is the fugacity of the CO_2 in the gas phase. The dissolved CO_2 dissociates and produce bicarbonate and carbonate ions:

$$CO_{2(aq)} + H_2O \rightleftharpoons H^+ + HCO_3^-, \quad pK_1 = 6.37 \tag{36}$$

$$HCO_3^- \rightleftharpoons H^+ + CO_3^{2-}, \quad pK_2 = 10.25 \tag{37}$$

The forward reaction constant values for the reactions (36) and (37) are $k_{CO_2} = 3.71 \times 10^{-2}$ s^{-1} and $k_{HCO_3^-} = 59.44$ s^{-1}, respectively. Water ionization was also taken into account:

$$H_2O \rightleftharpoons H^+ + OH^- \tag{38}$$

with the forward reaction constant being 2.4×10^{-5} mol L^{-1} s^{-1} and the equilibrium constant $K_w = 10^{-14}$ mol^2L^{-2}. In this study, Authors investigated different reaction mechanisms for the CO_2 reduction half-reaction with the aim of predict the CO and hydrogen production. In particular, the reaction mechanism reported in Fig. 6 was assumed to be the most likely where the formation of the **COOH intermediate is the most probable rate limiting step.

Eqs. (23)–(25) as well as the Nernst-Plank equations (Eqs. (50) and (51)) represent a convenient compromise between accuracy and computational demand to merge in a single description all the relevant multi physics phenomena occurring at different time scales in photo(electro)chemical devices. Those continuum models are used not only in the field of photochemistry, but also in other circumstances where mass and charge transport is coupled with chemical reactions, as occurs in fuel cells [139,140]. Other methods are being developed to consider in detail the nanoscopic nature of the matter and how it influences chemical reactions, for example molecular dynamics with machine learning force-fields [141] or with reactive force-fields (ReaxFF) [142]. However, nowadays, these approaches are limited and tailored to some specific systems [143,144]. Moreover, coupling the molecular time scales (in the order of pico to nanoseconds) to processes occurring at higher scales such as convection (seconds to minutes) still remains a major challenge [145].

3. Physical phenomena: describing the local environment of reactive interfaces

The arrangement of photoactive molecules is reported to be one of the factors which contributes to an efficient light harvesting and energy and electron transfer in supramolecular assemblies [89,155]. Chen and coworkers [156] demonstrated how ruthenium based dyes anchored on a titania nanoparticle were able to self-exchange electrons and oxidize a distant co-anchored catalyst. Other authors demonstrated [76,111] how the same molecules behave differently if enclosed in a molecular scaffold such as liposomes with respect to homogeneous conditions. Analyzing the three steps of photoxidation of water reported in Section 1.1, Authors in [111] discovered that the rate determining step in homogeneous condition is the second step (electron transfer from the catalyst to the PS), while if the same photoactive molecules are enclosed in a liposome, step 1 (electron transfer from the PS to the electron acceptor) becomes rate determining. This was attributed by a improved electron transfer kinetics between the PS and catalyst embedded in the membrane. Moreover, the performance of these systems was found to be dependent on the type of lipid that constitutes the liposomes [157]. Other researchers focused on the effect of the base surfactant on photochemical hydrogen production in micelles. In particular, positively charged iridium based photosensitizers and cobalt based catalysts were reported to behave more efficiently in a cationic micellar media than in nonionic or anionic micellar media [78]. Studies on the effect of the self-assembling of photoactive molecules at air–water [158–160] or solid-water interface [161,162] have also been performed. An extensive characterization of porphyrin monolayers with and without alkyl tails and mixed with and without surfactants was carried out by Viseu and coworkers [163], who proposed a possible structure of the mixed surfactant-porphyrin monolayers and measured the self-quenching efficiency of the porphyrins in the different systems. Authors found that the quenching efficiency of the alkylated porphyrin was higher in systems with cationic surfactants. Moreover, monolayers containing the alkylated porphyrins were generally more stable than then their counterparts containing non-alkylated porphyrins. Similarly, an improvement of the reaction owing to the self-assembled structures with respect to homogeneous conditions was observed by Wang et al. [82] who studied water oxidation to oxygen using a tin porphyrin as photocatalyst and a cobalt based electron acceptor in the absence and presence of surfactants.

In this section, we summarize some techniques useful to investigate the morphological structure of liposomes, monolayers and micelles as well as the effect of charged surfaces immersed in a solution containing electrolytes and how they influence the photochemical reactions (see Fig. 7).

3.1. Atomistic and coarse-grained models

We focus on atomistic and coarse-grained (CG) simulation for the application of interest. We stress that a comprehensive review of the CG models is beyond the scope of this manuscript. For a more detailed review of such tools, the interested reader is delegated to other specific publications [164–168]. Several modeling tools have been developed during the decades by researchers to investigate properties of surfactant systems [147] and summarized in Table 4. Atomistic simulations can be usually employed to study the dynamics of the surfactants and water and their interactions with other molecules such as gases in monolayers and soap films [146,148,154,169]. While atomistic models are accurate to describe pico to nanoseconds system variations in nanometers scale systems, they often become too computationally demanding to investigate processes such as agglomeration, phase transitions, and self-assembly that require large time scales and system sizes. CG models might be a solution to investigate such systems. In CG models molecules are represented as groups of atoms (beads), rather than individual atoms. So, a considerable number of degrees of freedom of the atomistic simulations is eliminated, allowing for simulation of larger systems and longer time scales. The trade-off for the increased efficiency is a loss of accuracy, as the details of inter-atomic interactions are not fully represented. In summary, the main difference between coarse-grained and atomistic simulations is the level of detail in the representation of the system and the corresponding trade-off between

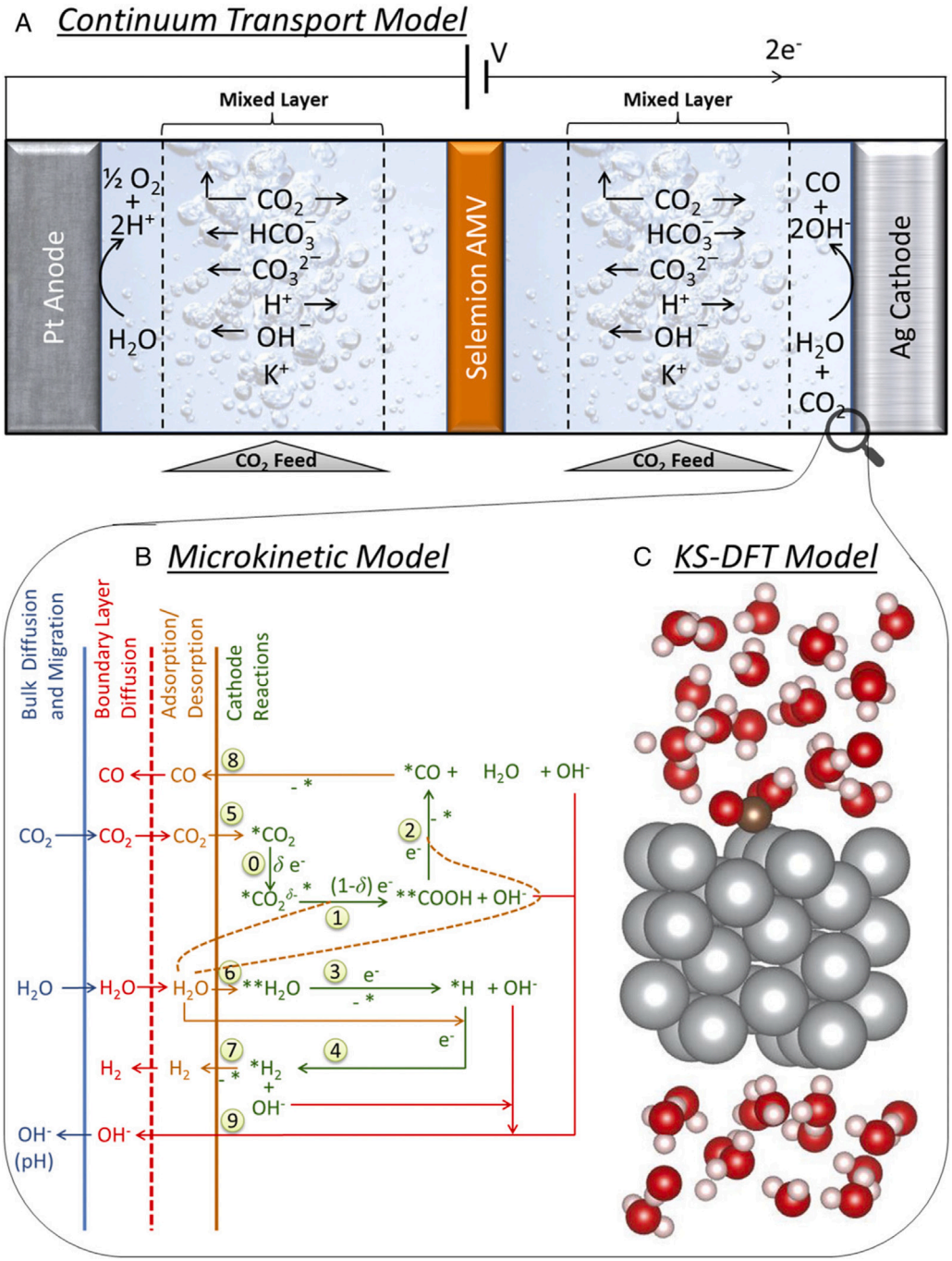

Fig. 6. Multiscale model for electroreduction of CO on Ag electrodes. (A) Continuum model for species transport and reactions (electrochemical reaction at the electrode interface and chemical equilibria in the bulk) in a 1D electrochemical cell. An anion exchange membrane "Selemion AMV" [138] separates the two compartments. (B) The proposed microkinetic model of the CO_2 and hydrogen evolution reactions on the silver electrode considers adsorption and desorption of reactants and products as well as the elementary surface reactions. The proposed mechanisms has 8 species and ten elementary reactions: the carbon dioxide reduction is represented by reactions 0, 1, 2; proton reduction is described by reactions 3 and 4; 5, 6, 7 and 8 are adsorption–desorption reactions; reaction 9 represents the release of OH^- to the bulk. (C) A DFT model is used to calculate the energies of adsorption, reaction intermediates and reaction barriers for the microkinetic model.
Source: [96].

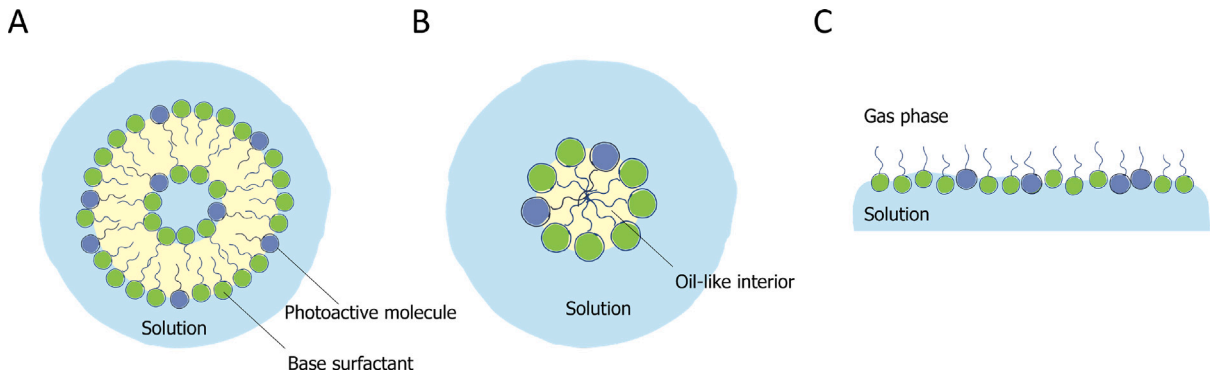

Fig. 7. Examples of self-assembled structures: (A) liposome, (B) micelle, (C) monolayer. Base surfactant is depicted in green, while the photoactive molecule is violet colored. Note that this is a schematic representation, the photoactive molecule could be at the surface of the structure as well as deep inside the oil-like interior [76,77].

Table 4
Main categories of models for describing physical phenomena in photo(electro)chemical devices.

Model category	General description	Advantages and main use	Disadvantages	Main Refs.
Atomistic models	In these discrete models, atoms interact through energy potentials (e.g. Coulombic, Lennard-Jones). In the case of classical Molecular Dynamics, particles evolve dynamically over time following the Newton's law of motion. For Monte Carlo based simulations consistent microstates corresponding to a chosen set of observables are obtained.	• Studying molecular scale phenomena (water-surfactant interactions, gas adsorption, electric double layer formation). • Detailed analysis of interfaces. • Prediction of macroscale properties from nanoscale details.	• Complex potential with many fitting parameters (ex. ReaxFF reactive force-field) are necessary to describe the reactions. . • Short time and space scales are observable. • High computational cost.	[142,146–148]
Coarse grained models	In these discrete models, atoms are grouped in single beads that interacts through energy potential.	• Simulation of larger systems for longer times than atomistic models. • Studying mesoscale structures and phenomena such as the self-assembling of molecules and the attachment of molecules on a matrix.	• Details of inter-atomic interactions are not fully represented. • Difficulties in describing chemical reactions. • High computational cost	[149–151]
Macroscale continuum models	See also Table 3	These models merge in a multi-physics framework the simulation of both chemical and physical phenomena, see also Table 3.	See also Table 3	[33,96,97]
Thermodynamic relations/equations of state	The system is described by thermodynamic relations/equations of state.	Understanding the thermodynamic equilibrium of a system, e.g.: • How the surface composition at the water surfactant air interface depends on the bulk concentration of surfactants using the various adsorption isotherms and equations of states (Van der Waals, Volmer...). • The micellization process and the shape of aggregates.	• Often many fitting parameters are required.	[152–154]

accuracy and computational efficiency [164]. CG models have been successfully used for studies on bilayers [170,171], monolayers [150], micelles [172] and vesicles [149]. These models are enough accurate to investigate the formation and equilibration of large surfactant systems for example for the case of phase diagrams of monolayers or micelles dynamics [147,172] as shown in Fig. 8. Duncan and coworkers [150] used the Martini force field to simulate the different transition phase of a monolayer of lung surfactants with additional molecules such as peptides. Other Authors [151] developed a multiscale model where a CG Monte Carlo model is coupled with atomistic simulations by a force matching procedure. The CG model was then used to calculate the gas and liquid phases of the monolayer.

Photoactive molecules [82,89,173] are fairly complex molecules and require different modeling tools in order to coherently describe their behavior in self-assembled structures [165,174]. Some CG models have been developed for investigating drug delivery processes as these simulations allow to simulate the evolution of lipid systems in the microseconds time scale [175,176]. Photoactive amphiphilic porphyrins were studied by Wang and coworkers [177] as a basis to form supra-molecular assemblies with the final aim of making an efficient photochemotherapy based anticancer treatment. Dissipative particle dynamics (DPD) simulations were used to investigate the process of micelles and nanoparticle formation and for a rational design of the supramolecular assembly as shown in Fig. 9. Similar porphyrins are

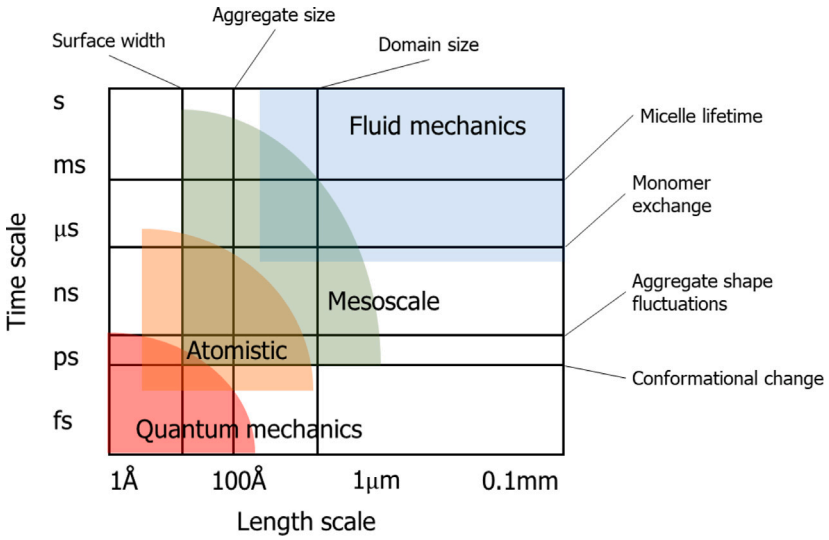

Fig. 8. The Log-Log plot reports various models available and the different time and space scales they can investigate. Atomistic simulations can be used to study micelle shape fluctuations, surfactant orientation, ion association and water dynamics. The investigation of micellar aggregation or phase formations in monolayers require mesoscale coarse-grained models.
Source: Adapted from [147].

used for light harvesting [178] and catalysis [179]. CG simulations were used by Sai et al. [180] to understand how the light harvesting amphiphilic molecules (perylene monoimide) self-assemble and attach in a hydrogel matrix. Authors demonstrated how this light harvesting composite in solution with a proton reduction catalyst ($Na_2[Mo_3S_13]$) was able to produce hydrogen under light irradiation. Authors in [181] developed a CG Monte Carlo based model able to predict the surface tension and the arrangement of photoactive molecules at the water-gas interface with a few parameters easily obtainable from experiments or atomistic simulations. Authors then related the predicted structure of the monolayer with the reaction constants of water oxidation and CO_2 reduction.

3.2. Thermodynamics of self-assembled structures

Along with the particle based simulations, thermodynamic theories are a useful tool to investigate the self-assembling of amphiphilic molecules for example to understand the number of molecules at the interfaces or the shape of the aggregates they are forming. Several theories have been developed over the decades [152]. Most of the models refer to the surface tension as physical observable corresponding to the morphological structure at the nanoscale of the water-surfactant-air interface. The surface tension decreases as more surfactants are added to the solution and diffuse to the interface until a certain threshold defined as critical micelle concentration or CMC (Fig. 10). Adding more surfactants does not have a significant effect on the surface tension, since the monolayer at the surface is saturated and the surfactants aggregate in solutions forming micelles. Two main approaches can be followed to treat the adsorption at the gas–liquid (or liquid–liquid) interfaces. From one side, adsorption is treated as an equilibrium phenomenon determined by the laws of thermodynamics. In the second approach, the surfactant monolayer is treated as a layer with a surface pressure and a surface excess related by an equation of state [182]. The Gibbs adsorption isotherm belongs to the first class and the simplest case is its adoption to a system of two components, the solute (the surfactants in this case) and the solvent. The isotherm relates the surface concentration of the surfactant (excess surface concentration, Γ) to the variation of the surface tension, γ, as follows:

$$\Gamma = -\frac{1}{mRT}\left(\frac{d\gamma}{d\log(a)}\right) \tag{39}$$

Table 5
Packing parameter value and corresponding type of aggregate.

Packing parameter	Shape of the aggregate
$0 < v_0/a_e l_0 < 1/3$	Sphere
$1/3 < v_0/a_e l_0 < 1/2$	Cylinder
$1/2 < v_0/a_e l_0 < 1$	Bilayer

being a the activity of the surfactant in the bulk solution calculated as the concentration of the surfactant multiplied by the activity coefficient, $m = 1$ for non-ionic surfactants or ionic surfactants in the presence of a large excess of salt and $m = 2$ for ionic surfactants. An example of adsorption isotherm is reported in Fig. 10. The process of micellization is driven by two counter acting factors. On the one hand, the transfer of the hydrocarbon chain of the surfactant from the aqueous phase in solution to the inner part of the micelle is associated with an entropic effect. This entropic effect is related to the water molecules around the surfactant tail that are highly ordered, so when the hydrocarbon chains are located inside the oil-like interior of the micelles, the entropy of water increases [183]. Indeed, it is observed experimentally that longer tails in the same surfactant reduce its CMC [152]. On the other hand, the polar head groups of the surfactants repel each other as they come closer thus opposing to the aggregation process. An additional repulsion force is present for the case of charged surfactants [183].

The structure of the micelles can be predicted from the geometry of the surfactant molecules and estimated on the basis of the packing parameter $v_0/a_e l_0$, being v_0 and l_0 the volume and the length of the surfactant tail and a_e the area per molecule of the surfactant. Depending on the value taken by the packing parameter, the probable shape of the aggregate is shown in Table 5[152,153]. The main unknown parameter is the area per molecule, which is not simply connected to the geometrical size of the surfactant head group, but rather a thermodynamic quantity derived from equilibrium consideration of the free energy. In its classic representation, it is defined as:

$$a_e = \left(\frac{\alpha}{\sigma_e}\right)^{1/2} \tag{40}$$

where α considers the head group interactions, σ_e is the contact free energy per unit area (or interfacial free energy). The size of micelles varies depending on the surfactant and the solution (water or mixtures,

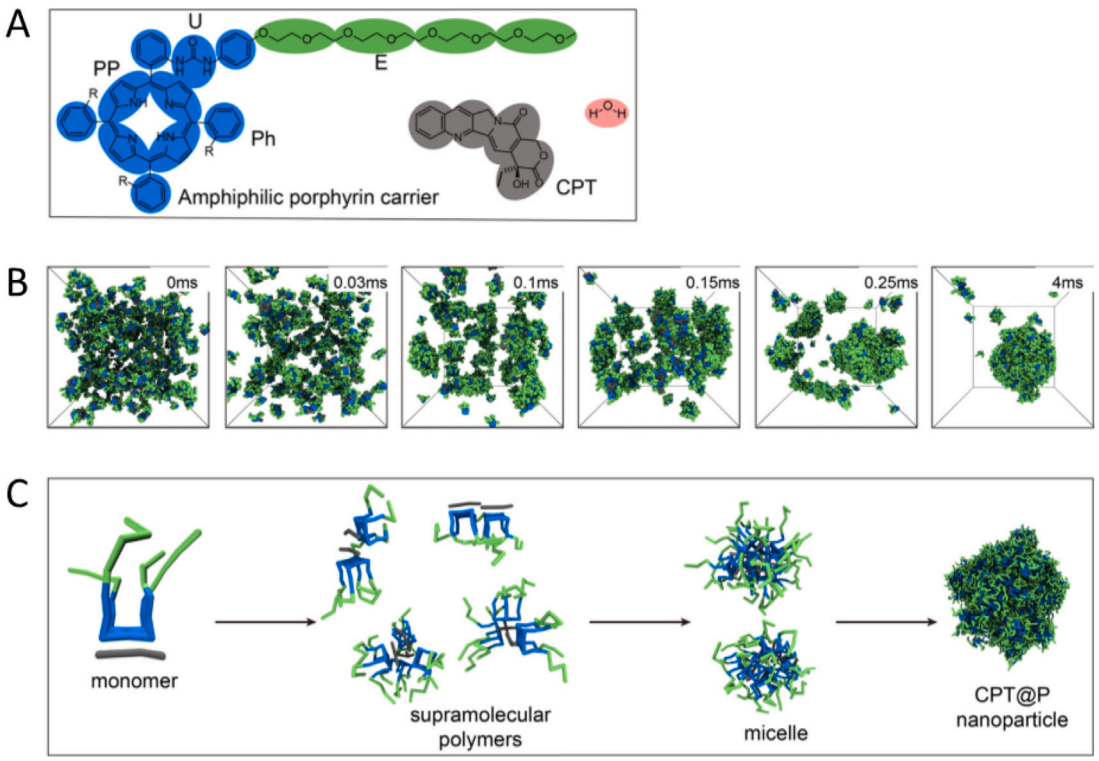

Fig. 9. Example of coarse-grained amphiphilic porphyrins and their self-assembling. (A) All atom and coarse-grained model of the amphiphilic porphyrin photosensitizer, camptothecin (CPT) and water. In the CG model, water is represented as a single particle and CPT is divided in four beads. The amphiphilic porphyrin is coarse-grained using four types of beads representing the porphyrin plane (PP), the phenyl ring (Ph), the urea group (U) and the hydrophilic ether groups (E). (B) Snapshots showing the formation of particles starting from the monomers reaching the final spherical structure. At the beginning CPT and the porphyrin form an amphiphile structure owing to $\pi - \pi$ stacking, hydrogen bonding and hydrophobic interaction. These monomers self-assemble in clusters, which associate in larger assemblies to finally rearrange in a nanoparticle. (C) The schematic representation of the nanoparticle formation: stage 1, monomer formation; stage 2, irregular assemblies formation, stage 3 large assemblies formation; stage 4, nanoparticle formation.
Source: Adapted from [177].

salt concentration). The diameter of a typical micelles is in the order of 3 to 6 nm [183].

Among the different adsorption isotherms, we present here the Frumkin equation for nonionic surfactants [184], which can be easily extended to multi-component mixtures as shown in the following paragraph. The adsorption isotherm, Eq. (41), is obtained by coupling the surface pressure isotherm (Eq. (42)) with the Gibbs adsorption equation:

$$ba = \frac{\theta_i}{1-\theta_i}\exp(-2\beta\theta_i) \tag{41}$$

$$\pi = -\frac{RT}{\omega_\Sigma}(\log(1-\theta_i) + \beta\theta_i^2) \tag{42}$$

where b is the adsorption constant, $\theta_i = \Gamma_i\omega_\Sigma$ the surface coverage, ω_Σ is the average of the partial molar area of all components (for one surfactant it is the molar area of the surfactant) and can be viewed as a parameter which considers the excluded area per molecule, β takes into account the interactions between the adsorbed molecules. The parameters ω_Σ and β, for the Frumkin as well as for other adsorption isotherms such as the Van der Waals adsorption isotherm, can be obtained either by fitting experimental data [182] or from numerical simulations [185]. For example, in the works of Blankschtein and coworkers [186,187] various characteristics (micelle shapes, critical micelle concentration, surface concentration) of surfactant systems were estimated by coupling thermodynamic relations with computer simulations. We reported so far the case of a single type of non ionic surfactant, however adsorption isotherms for multicomponent systems have been developed [188–190]. Fainerman et al. [190] generalized the Frumkin adsorption equation for a mixture of two non ionic surfactants. Eqs. (41) and (42) are rewritten as:

$$b_i a_i = \frac{\theta_i}{1-\theta_1-\theta_2}\exp(-2\beta_i\theta_i - \beta_{12}\theta_j) \tag{43}$$

$$\pi = -\frac{RT}{\omega_\Sigma}(\log(1-\theta_1-\theta_2) + \beta_1\theta_1^2 + \beta_2\theta_2^2 + \beta_{12}\theta_1\theta_2) \tag{44}$$

where the subscripts 1 and 2 indicate the surfactant 1 and the surfactant 2 and i the surfactant type (1 or 2). Other theories for describing insoluble monolayers [191] or insoluble monolayers penetrated by soluble surfactants [192] have been also developed.

3.3. The electric double layer

Charged colloids and electrodes such the ones mentioned so far have a significant impact on the electrolyte solution owing to the electrostatics interactions. The layer of surface charges and the attracted counterions is called electric double layer. This is a relevant phenomenon since the photocatalytic reactions occur in the first nanometers from the charged surface both in the case of the electrodes or colloids. Indeed, the interactions between the reactive and non-reactive species and the catalyst surface have direct influence on the activity and selectivity of the catalyst [193]. The Helmholtz layer is the simplest model of an electric double layer. It consist of counterions directly attached which neutralize the charged surface as in a plate capacitor. A more detailed model was introduced by Gouy and Chapman who included the thermal agitation of the counterions close to charged flat surfaces predicting a diffuse layer. These theories consider the solvent as a continuum mean defined by a relative permittivity ignoring the molecular nature of the liquid. Moreover, the ions are treated as a continuous charge distribution and not as individual charges. The electric potential V near

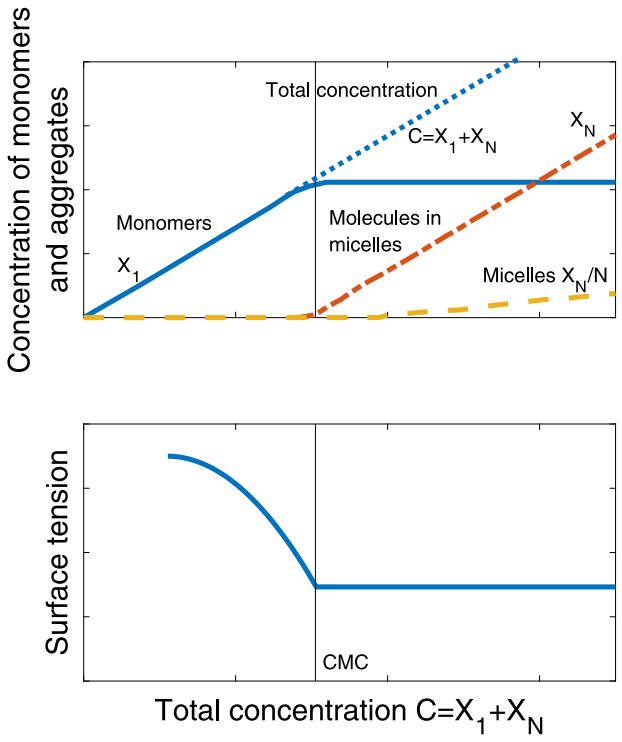

Fig. 10. Top panel: concentration of monomers, X_1, and aggregates (micelles), X_N, as function of the total concentration of surfactants. N_m is the aggregation number, namely the number of molecules per aggregate. Bottom panel: surface tension as function of the total concentration. The surface tension reaches a pleateu when the surfactant concentration is at the CMC (critical micelle concentration). At CMC, aggregates start forming and the number of monomers is nearly constant both in the bulk and at the surface. So, that the surface concentration of monomers and thus the surface tension remain constant.
Source: Adapted from [152].

a charged interface is described by the Poisson–Boltzmann equation. We report the general solution for the full Poisson–Boltzmann equation in the case of planar surfaces and 1:1 electrolyte [183]:

$$e^{y/2} = \frac{e^{y_0/2} + 1 + (e^{y_0/2} - 1)\cdot e^{-\kappa x}}{e^{y_0/2} + 1 - (e^{y_0/2} - 1)\cdot e^{-\kappa x}} \tag{45}$$

where $y = eV/k_BT$ is the dimensionless potential and κ is the inverse of the Debye length defined as:

$$\kappa = \left(\frac{2c_0e^2}{\epsilon\epsilon_0 k_B T}\right)^{1/2} \tag{46}$$

The Grahame equation correlates the surface charge σ and the potential at the electrode V_0 based on the Gouy-Chapman theory of the diffuse double layer:

$$\sigma = (8c_0\epsilon\epsilon_0 k_B T)^{1/2}\cdot \sinh\left(\frac{eV_0}{2k_BT}\right) \tag{47}$$

The Stern theory combines the Helmholtz layer with the diffuse layer. Stern envisioned a first layer of adsorbed ions that are immobile, while the ions further away from the surface behave following the Poisson–Boltzmann statistics. The simplest case of Stern layer is the one that consider the finite size of the counterions. Thus, the electric potential drops linearly in the Stern layer following:

$$V_\delta = V_0 - \sigma\frac{\delta}{\epsilon_\delta\epsilon_0} \tag{48}$$

where δ is the radius of the hydrated ion. The three models of the electric double layer presented are summarized in Fig. 11.

Numerical solution for the analysis of the electric double layer can be found in literature [98,194]. The charge density is related to the electric potential by the Poisson equation:

$$\nabla^2 V = \frac{\rho_e}{\epsilon\epsilon_0} \tag{49}$$

where ρ_e is the electric charge density, ϵ the permittivity of the mean and ϵ_0 the permittivity of vacuum. The transport of charged species in solution is usually described by the Nernst–Planck equation:

$$\frac{\partial c_i}{\partial t} + \nabla\cdot\mathbf{J}_i = S_i \tag{50}$$

$$\mathbf{J}_i = -D_i\nabla c_i - \frac{D_i Z_i F c_i}{RT}\nabla V + c_i\mathbf{u} \tag{51}$$

where V is the electric potential, c_i is the bulk concentration of the ith species, $\mathbf{J_i}$ the molar flux, S_i a source term related to chemical reactions, D_i the diffusion coefficient in water, Z_i the valence of the ionic species, T the absolute temperature, F the Faraday constant and R the universal gas constant. The last term, $c_i\mathbf{u}$, is not zero in the case of a convective flux of velocity $\mathbf{u}$. The numerical solution of the Nernst–Planck equation (Eqs. (50) and (51)) coupled with the Poisson equation (Eq. (49)) was used to calculate the diffuse electric double layer generated by the surfactants layers of a soap film in [181]. A similar approach was adopted by Bohra and coworkers [98] who studied the electroreduction of the CO_2 at a generic planar cathode in the presence of an electrolyte. Authors considered a Stern layer close to the electrode (0.4 nm). Then they analyzed the diffuse layer by considering the effect of the ions size by using the generalized modified Poisson-Nernst-Plank model (GMPNP). In the GMPNP, Eq. (51) is rewritten to account for the effective solvated diameter of the species i, d_i:

$$\mathbf{J}_i = -D_i\nabla c_i - \frac{D_i Z_i F c_i}{RT}\nabla V - D_i c_i\left(\frac{N_A\sum_{i=1}^{n_s} d_i^3\nabla c_i}{1 - N_A\sum_{i=1}^{n_s} d_i^3\nabla c_i}\right) \tag{52}$$

where n_s is the number of species i in solution. Note that the convective term is neglected in Equation (52). Furthermore, the permittivity ϵ in Eq. (49) was assumed to be dependent on the electric field:

$$\epsilon = \epsilon_r\left(\frac{M_{water} - \sum_{i=1}^{n_{cat}} w_i c_i}{M_{water}}\right) + \epsilon_{min}\left(\frac{\sum_{i=1}^{n_{cat}} w_i c_i}{M_{water}}\right) \tag{53}$$

where M_{water} is the molar concentration of water (55 M at 25 °C), w_i is a parameter related by the number of water molecules held by the ion i, $\epsilon_r = 80$ is the relative permittivity of water and ϵ_{min} is the relative permittivity of confined water assumed to be 6. This equation thus considers the contribution of the bulk and of the cation-bounded water molecules to calculate an effective concentration dependent relative permittivity ϵ. Finally, the reaction equilibria of the CO_2 in solution was taken into account together with an imposed current density; the latter directly acting on the CO_2 reaction kinetics. Authors were able to understand the effect of different ions, of the pH and of the current density on the CO_2 concentration at the interface, thus, on the CO (and hydrogen) production. For example, the presence of Cesium and Potassium cations resulted in a stronger electric field at electrode interface. Thus, the experimental evidence of performance improvement in the presence of Cesium might be related not only to the electric field strength but also to the specific ion interactions [98].

Numerical models based on the simulation of discrete ions with implicit or explicit water have been developed, both through grand canonical Monte Carlo (GCMC) [195] and molecular dynamics (MD) simulations [196,197]. We report in Appendix a primitive GCMC model of the electric double layer for a planar surface inspired by the seminal work of Torries and Valleau [195,198]. In Fig. 12, the concentration of the ions close to a charged planar surface is reported. The solution from the GCMC simulations matches the analytical solution of the Poisson–Boltzmann equation (Eq. (45)) for a low concentration of electrolyte (10 mM) and a low surface charge of 0.010 C m^{-2} corresponding to a surface potential, calculated with Eq. (47), of 0.04 V. For higher concentration of salt, the GCMC results slightly deviate form the analytical solution since the particles are solid spheres with

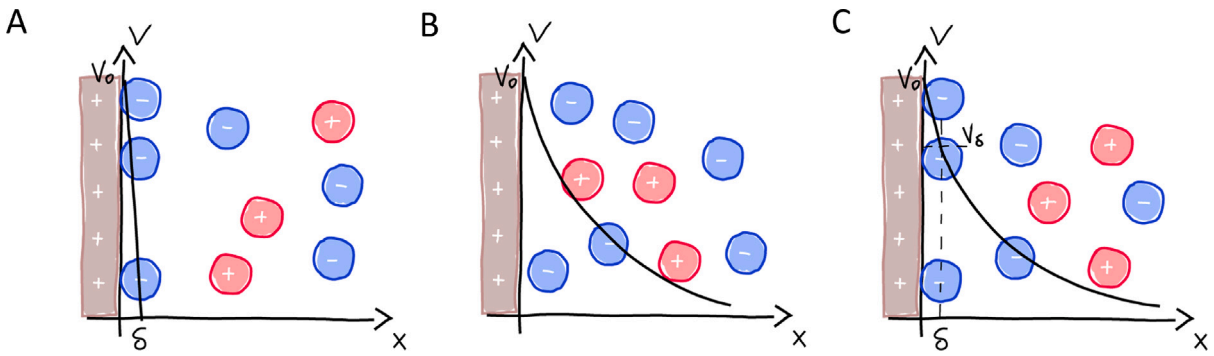

Fig. 11. Different models for the electric double layer. The electric potential along with a qualitative distribution of the ions is depicted. The charged surface is gray colored, cations are red and anions blue. (A) Helmholtz model. (B) Gouy-Chapman model of the diffuse double layer. (C) Stern model.

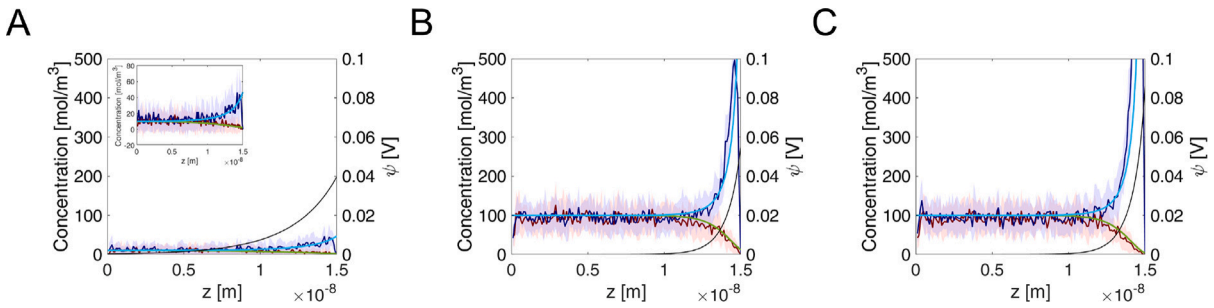

Fig. 12. GCMC simulation results for a 1:1 electrolyte solution close to a charged planar surface. The dark blue and dark red curves show the ions concentration resulted from the GCMC simulations. The light blue and light green curve represent the ions distribution along with electric potential (black curve) obtained from the analytical solution of the Poisson–Boltzmann equation (Eq. (45)). (A) Electrolyte concentration of 10 mM and surface charge for 0.010 C m^{-2}. (B) Electrolyte concentration of 100 mM and surface charge for 0.048 C m^{-2}. (C) Electrolyte concentration of 100 mM and surface charge for 0.096 C m^{-2}.

a diameter (0.36 nm for the Sodium and 0.33 nm for the Chloride ions [152]) and the interaction energy between the ions is considered in the numerical solution unlike in the Poisson–Bolzmann equation. We report in Fig. 12 the comparison at high concentration of electrolyte (100 mM) and at high surface charge of 0.266 C m^{-2} corresponding to a surface potential of 0.19 V. This model could be further developed to simulate more complex interfaces as well as multivalent ions [199] or variable permittivity [200].

4. Conclusions and discussion

Multi-scale and multi-physics modeling tools are essential to describe and understand the multiple processes occurring at the different time and space scales in devices for the photochemical production of fuels. To this end, both continuum and discrete models can be applied and coupled together to study the disparate number of involved phenomena. We reviewed different tools for investigating the various steps of photo-chemical reactions. We investigated light absorption and electron–hole formation as well as their diffusion in electrodes or nanoparticles. Possible coupling between equilibrium reactions in solution and diffusion phenomena together with the photochemical reactions in a multiphysics framework were proposed. Atomistic and coarse-grained models as well as thermodynamic relations were reviewed to critically discuss the self-assembling of photoactive molecules in supra molecular aggregates, which is reported to be one of the key factor for an efficient photochemical reaction. Finally, a focus on the local environment close to a charged surface was given. In this respect, the electric double layer is identified as ubiquitous and crucial in photo(electro)chemistry and in the presence of a polar solvent. In general, considerable room for improvement is foreseen for photochemical devices for fuel production, as this technology is still in early stage of research, and theoretical modeling can be a valid support for their optimization. The intrinsic multiphysics and multi-scale nature of the photochemical phenomena pose new challenges for their modeling, which require new approaches and strategies to be effectively addressed. Based on the above overview from the current literature, we believe that both bottom-up and top-down strategies are requested to tackle the formidable challenges and knowledge gaps. Specifically focusing on bottom-up approaches and the chemical phenomena summarized in Table 3 a detrimental lack of model coupling at different scales has been found. Attempts in this respect as the one reported in Fig. 6 from [96] are certainly of great value and very encouraging, but still limited to very specific cases and often rely on handcrafted coupling attempts with limited accessibility to most of the pertinent scientific community. In this sense, we believe that a larger community effort is requested in the near future to build up well structured tools describing phenomena at different space and time scales, ideally fully integrated within established computational environments (e.g. ASE [201]), capable of exchanging relevant parameters in an automated fashion and also complying with FAIR principles [202], with a special focus on the principles of findability and accessibility of data.

On the other hand, concerning the physical models summarized in Table 4, it is fair to say that we still lack some understanding of the laws governing molecular self-assembly. Shedding more light on such knowledge gap may open new opportunities to precisely design better local environments for photo-chemical systems. To this end, while experimental capabilities remain certainly scientifically invaluable, atomistic computational models are unique in their ability to serve as microscopes with great resolution and observability. Unfortunately, functionality of self-assembled aggregates includes phenomena with time scales ranging from nanoseconds to seconds. Coping with such an intrinsic multi-scale character is currently out of reach for direct atomistic simulations. To overcome this impasse, we believe that new advances in data mining and deep learning to significantly accelerate atomistic models can play a critical role in the near future [203]. Furthermore, even when atomistic and coarse-grained models can be used to simulate how catalysts and photosensitizers self-assemble, it

is worth reminding that those models are often tailored to reproduce some features of a specific system and may require re-parametrization to describe similar phenomena in other systems or in other thermodynamic conditions [204–206]. Moreover, the arrangement of photoactive molecules is only a part of the many factor influencing the stability of the compounds and the reaction efficiency. The large number of variables (species concentrations, temperature, pressure and surface characteristics) in experiments as well as in simulations results in a high dimensional space to explore. In perspective, we believe that at least two aspects have to be more properly addressed in future research. In this respect, the use of both detailed quantum computations and the most advanced characterization techniques, such as non linear spectroscopy, are expected to shed more light on the underling fundamental processes behind photochemical generation of solar fuels. In particular, an important aspect that still remains to be clarified, especially using quantum computations, is the possibility of exploiting the incredibly high electric fields [169] at gas–liquid reactive interfaces to possibly enhance photochemical and photoelectrochemical processes. Furthermore, it is desirable to develop more detailed kinetic mechanisms similarly to the progresses we have witnessed in the past in other fields (e.g. detailed combustion mechanisms [207–209]).

Finally, we stress that the number and complexity of phenomena to be described in such photo-chemical and photo-electrochemical systems is such that algorithmic top-down optimization approaches are also welcome in the field. In this respect, we believe that, a key contribution could come in the near future from sequential and machine learning algorithms that could help in effectively orchestrating experimental campaigns as well as simulations [210,211]. Interestingly, such approaches could be used not only for design and optimization of the operating conditions in specific conditions, but also for gaining insights on the most important features ruling photo-chemical and photo-electrochemical systems and technologies. To this end, feature importance (such as the SHAP analysis [212]) or feature grouping analysis [213] could play an important role. Finally, more holistic approach considering experiments and modeling combined with artificial intelligence to optimize the already existing systems and materials as well as to discover new materials [214] might be a further step to solve the various challenges in the photo(electro)catalytic reduction of CO_2.

The authors declare the following financial interests/personal relationships which may be considered as potential competing interests: Eliodoro Chiavazzo reports financial support was provided by European Commission.

Data availability

We make available via public platforms (i.e. Zenodo, Github) codes for simulating ion distribution close to a charged surface (see manuscript).

Acknowledgment

This work has been funded by the European Commission in the framework of the project SoFiA—Soap Film based Artificial Photosynthesis—grant agreement 828838.

Appendix. The GCMC algorithm

We considered a 1:1 electrolyte in water with a relative permittivity $\epsilon = 80$. The ions are treated as hard spheres with a diameter d_c and d_a for the cations and the anions, respectively, interacting through electrostatic potential:

$$U_{ij}(r) = \frac{q_i q_j}{4\pi\epsilon\epsilon_0 x} \tag{A.1}$$

being q_i and q_j the charge of the ions i and j and x their distance. The Monte Carlo algorithm proceeds by inserting, deleting or translation the particles in the simulation box in the μVT ensemble. The acceptance probability for the insertion move is the following:

$$P_a = \frac{e^{B-\Delta U/k_B T}}{(N^+ + 1)(N^- + 1)} \tag{A.2}$$

where ΔU is the energy difference between the two microstates before and after the insertion, N^+ is the number of positive ions, N^- the number of negative ions and B is defined as:

$$B = 2(\log(\gamma_\pm) + \log(Vol\rho)) \tag{A.3}$$

being $\gamma_\pm$ the activity coefficient of the electrolyte (it can be assumed nearly 1 for dilute solutions), Vol the volume of the simulation box and ρ is the target number density. Similarly the acceptance probability for the deletion (P_d) and the translation (P_t) moves are the following [195,198]:

$$P_d = \frac{1}{P_a} = \left(\frac{e^{B-\Delta U/k_B T}}{(N^+ + 1)(N^- + 1)}\right)^{-1} \tag{A.4}$$

$$P_t = \frac{e^{-\Delta U/k_B T}}{N^+ N^-} \tag{A.5}$$

The algorithm of the GCMC can be summarized as follows:

1. Randomly choose to insert, remove or translate a pair of ions;
2. Compute the energy variation ΔU of the system due to the decided move;
3. Compute the probability of retaining the inserted particles, namely: P_a, P_d or P_t for addition, deletion or translation;
4. Draw a random number from 0 to 1 ;
5. Accept if the probability is higher than the random number, else reject;
6. If the target number of iterations imposed is not yet achieved, re-start from step 1, else terminate the procedure.

The MATLAB® scripts of the GCMC algorithm as well as the analytical solution of the Poisson–Boltzmann equation are reported at [215,216].

References

[1] Carleton TA, Hsiang SM. Social and economic impacts of climate. Science 2016;353(6304):aad9837.
[2] Jacobson TA, Kler JS, Hernke MT, Braun RK, Meyer KC, Funk WE. Direct human health risks of increased atmospheric carbon dioxide. Nat Sustain 2019;2(8):691–701.
[3] Chatenet M, Pollet BG, Dekel DR, Dionigi F, Deseure J, Millet P, et al. Water electrolysis: from textbook knowledge to the latest scientific strategies and industrial developments. Chem Soc Rev 2022.
[4] Chiavazzo E. Looking for massive carbon capture. Nat Sustain 2023;1–2.
[5] UEIAdministration. International energy outlook 2021. 2021.
[6] IEA. World energy outlook 2022. 2022.
[7] Galan-Mascaros JR. Photoelectrochemical solar fuels from carbon dioxide, water and sunlight. Catal Sci Technol 2020;10(7):1967–74.
[8] Detz R, Reek J, Van Der Zwaan B. The future of solar fuels: when could they become competitive? Energy Environ Sci 2018;11(7):1653–69.
[9] Perez R, Perez M. A fundamental look at supply side energy reserves for the planet. Int Energy Agency SHC Program Sol Updat 2015;62:4–6.
[10] He J, Janáky C. Recent advances in solar-driven carbon dioxide conversion: expectations versus reality. ACS Energy Lett 2020;5(6):1996–2014.
[11] Møller KT, Jensen TR, Akiba E, w. Li H. Hydrogen-a sustainable energy carrier. Progress in Natural Science: Materials International 2017;27(1):34–40.
[12] Staffell I, Pfenninger S. The increasing impact of weather on electricity supply and demand. Energy 2018;145:65–78.
[13] Walter MG, Warren EL, McKone JR, Boettcher SW, Mi Q, Santori EA, et al. Solar water split cells. Chem Rev 2010;110(11):6446–73.
[14] Dincer I, Aydin MI. New paradigms in sustainable energy systems with hydrogen. Energy Convers Manage 2023;283:116950.
[15] Shin H, Jang D, Lee S, Cho H-S, Kim K-H, Kang S. Techno-economic evaluation of green hydrogen production with low-temperature water electrolysis technologies directly coupled with renewable power sources. Energy Convers Manage 2023;286:117083.
[16] Abe JO, Popoola A, Ajenifuja E, Popoola OM. Hydrogen energy, economy and storage: Review and recommendation. Int J Hydrogen Energy 2019;44(29):15072–86.

[17] Ishaq H, Dincer I, Crawford C. A review on hydrogen production and utilization: Challenges and opportunities. Int J Hydrogen Energy 2022;47(62):26238–64.
[18] Verma S, Lu S, Kenis PJ. Co-electrolysis of CO2 and glycerol as a pathway to carbon chemicals with improved technoeconomics due to low electricity consumption. Nat Energy 2019;4(6):466–74.
[19] Cuéllar-Franca RM, Azapagic A. Carbon capture, storage and utilisation technologies: A critical analysis and comparison of their life cycle environmental impacts. J CO2 Utiliz 2015;9:82–102.
[20] Tu W, Zhou Y, Zou Z. Photocatalytic conversion of CO2 into renewable hydrocarbon fuels: state-of-the-art accomplishment, challenges, and prospects. Adv Mater 2014;26(27):4607–26.
[21] Fu J, Jiang K, Qiu X, Yu J, Liu M. Product selectivity of photocatalytic CO2 reduction reactions. Mater. Today 2020;32:222–43.
[22] Habisreutinger SN, Schmidt-Mende L, Stolarczyk JK. Photocatalytic reduction of co2 on tio2 and other semiconductors. Angew Chem Int Ed Engl 2013;52(29):7372–408.
[23] Morris AJ, Meyer GJ, Fujita E. Molecular approaches to the photocatalytic reduction of carbon dioxide for solar fuels. Acc Chem Res 2009;42(12):1983–94.
[24] Chang X, Wang T, Gong J. Co 2 photo-reduction: insights into co 2 activation and reaction on surfaces of photocatalysts. Energy Environ Sci 2016;9(7):2177–96.
[25] Qiao J, Liu Y, Hong F, Zhang J. A review of catalysts for the electroreduction of carbon dioxide to produce low-carbon fuels. Chem Soc Rev 2014;43(2):631–75.
[26] Chu S, Ou P, Ghamari P, Vanka S, Zhou B, Shih I, et al. Photoelectrochemical co2 reduction into syngas with the metal/oxide interface. J Am Chem Soc 2018;140(25):7869–77.
[27] Shirazi A, Rahbari A, Asselineau C-A, Pye J. A solar fuel plant via supercritical water gasification integrated with fischer–tropsch synthesis: System-level dynamic simulation and optimisation. Energy Convers Manage 2019;192:71–87.
[28] Shih CF, Zhang T, Li J, Bai C. Powering the future with liquid sunshine. Joule 2018;2(10):1925–49.
[29] Badwal S, Giddey S, Kulkarni A, Goel J, Basu S. Direct ethanol fuel cells for transport and stationary applications–a comprehensive review. Appl Energy 2015;145:80–103.
[30] Zhu Z, Liu X, Bao C, Zhang K, Song C, Xuan Y. How efficient could photocatalytic co2 reduction with h2o into solar fuels be? Energy Convers Manage 2020;222:113236.
[31] Bondue CJ, Graf M, Goyal A, Koper MT. Suppression of hydrogen evolution in acidic electrolytes by electrochemical co2 reduction. J Am Chem Soc 2020;143(1):279–85.
[32] Hall AS, Yoon Y, Wuttig A, Surendranath Y. Mesostructure-induced selectivity in co2 reduction catalysis. J Am Chem Soc 2015;137(47):14834–7.
[33] Ahmed M, Dincer I. A review on photoelectrochemical hydrogen production systems: Challenges and future directions. Int J Hydrogen Energy 2019;44(5):2474–507.
[34] Zhang W, Jin Z, Chen Z. Rational-designed principles for electrochemical and photoelectrochemical upgrading of co2 to value-added chemicals. Adv Sci 2022;9(9):2105204.
[35] Wu H, Tan HL, Toe CY, Scott J, Wang L, Amal R, et al. Photocatalytic and photoelectrochemical systems: similarities and differences. Adv Mater 2020;32(18):1904717.
[36] Ola O, Maroto-Valer MM. Review of material design and reactor engineering on tio2 photocatalysis for co2 reduction. J Photochem Photobiol C Photochem Rev 2015;24:16–42.
[37] Zhang W, Mohamed AR, Ong W-J. Z-scheme photocatalytic systems for carbon dioxide reduction: where are we now? Angew Chem Int Ed 2020;59(51):22894–915.
[38] Uekert T, Pichler CM, Schubert T, Reisner E. Solar-driven reforming of solid waste for a sustainable future. Nat Sustain 2021;4(5):383–91.
[39] Yu J, González-Cobos J, Dappozze F, López-Tenllado FJ, Hidalgo-Carrillo J, Marinas A, et al. Wo3-based materials for photoelectrocatalytic glycerol upgrading into glyceraldehyde: Unravelling the synergistic photo-and electro-catalytic effects. Appl Catal B 2022;318:121843.
[40] Chaudhary YS. Solar fuel generation. CRC Press; 2017.
[41] Nielander AC, Shaner MR, Papadantonakis KM, Francis SA, Lewis NS. A taxonomy for solar fuels generators. Energy Environ Sci 2015;8(1):16–25.
[42] Reece SY, Hamel JA, Sung K, Jarvi TD, Esswein AJ, Pijpers JJ, et al. Wireless solar water splitting using silicon-based semiconductors and earth-abundant catalysts. Science 2011;334(6056):645–8.
[43] Giménez S, Bisquert J. Photoelectrochemical solar fuel production, from basic principle to advanced devices. Cham: Springer; 2016.
[44] Lidor A, Aschwanden Y, Häseli J, Reckinger P, Haueter P, Steinfeld A. High-temperature heat recovery from a solar reactor for the thermochemical redox splitting of h2o and co2. Appl Energy 2023;329:120211.
[45] Patel M, Zhang X, Kumar A. Techno-economic and life cycle assessment on lignocellulosic biomass thermochemical conversion technologies: A review. Renew Sustain Energy Rev 2016;53:1486–99.
[46] Sharma S, Basu S, Shetti NP, Aminabhavi TM. Waste-to-energy nexus for circular economy and environmental protection: Recent trends in hydrogen energy. Sci Total Environ 2020;713:136633.
[47] Huan TN, Dalla Corte DA, Lamaison S, Karapinar D, Lutz L, Menguy N, et al. Low-cost high-efficiency system for solar-driven conversion of co2 to hydrocarbons. Proc Natl Acad Sci 2019;116(20):9735–40.
[48] Temiz M, Javani N. Design and analysis of a combined floating photovoltaic system for electricity and hydrogen production. Int J Hydrogen Energy 2020;45(5):3457–69.
[49] Endrodi B, Kecsenovity E, Samu A, Darvas F, Jones R, Torok V, et al. Multilayer electrolyzer stack converts carbon dioxide to gas products at high pressure with high efficiency. ACS Energy Lett 2019;4(7):1770–7.
[50] Tong H, Ouyang S, Bi Y, Umezawa N, Oshikiri M, Ye J. Nano-photocatalytic materials: possibilities and challenges. Adv Mater 2012;24(2):229–51.
[51] Fujishima A, Honda K. Electrochemical photolysis of water at a semiconductor electrode. Nature 1972;238(5358):37–8.
[52] Tasleem S, Tahir M, Zakaria ZY. Z-scheme ag-nps-embedded lacoo3 dispersed pcn heterojunction with higher kinetic rate for stimulating photocatalytic solar h2 production. Energy Convers Manage 2022;266:115787.
[53] Call A, Cibian M, Yamamoto K, Nakazono T, Yamauchi K, Sakai K. Highly efficient and selective photocatalytic co2 reduction to co in water by a cobalt porphyrin molecular catalyst. ACS Catal 2019;9(6):4867–74.
[54] Dalle KE, Warnan J, Leung JJ, Reuillard B, Karmel IS, Reisner E. Electro-and solar-driven fuel synthesis with first row transition metal complexes. Chem Rev 2019;119(4):2752–875.
[55] Gupta A, Likozar B, Jana R, Chanu WC, Singh MK. A review of hydrogen production processes by photocatalytic water splitting–from atomistic catalysis design to optimal reactor engineering. Int J Hydrogen Energy 2022.
[56] Kamal KM, Narayan R, Chandran N, Popović S, Nazrulla MA, Kovač J, et al. Synergistic enhancement of photocatalytic co2 reduction by plasmonic au nanoparticles on tio2 decorated n-graphene heterostructure catalyst for high selectivity methane production. Appl Catal B 2022;307:121181.
[57] Dasireddy VD, Likozar B. Photocatalytic co2 reduction to methanol over bismuth promoted batio3 perovskite nanoparticle catalysts. Renew Energy 2022;195:885–95.
[58] Fan WK, Tahir M. Recent advances on cobalt metal organic frameworks (mofs) for photocatalytic co2 reduction to renewable energy and fuels: A review on current progress and future directions. Energy Convers Manage 2022;253:115180.
[59] Kuehnel MF, Sahm CD, Neri G, Lee JR, Orchard KL, Cowan AJ, et al. Znse quantum dots modified with a ni (cyclam) catalyst for efficient visible-light driven co 2 reduction in water. Chem Sci 2018;9(9):2501–9.
[60] Leung JJ, Warnan J, Ly KH, Heidary N, Nam DH, Kuehnel MF, et al. Solar-driven reduction of aqueous co2 with a cobalt bis (terpyridine)-based photocathode. Nat Catal 2019;2(4):354–65.
[61] Badiani VM, Casadevall C, Miller M, Cobb SJ, Manuel RR, Pereira IA, et al. Engineering electro-and photocatalytic carbon materials for co2 reduction by formate dehydrogenase. J Am Chem Soc 2022;144(31):14207–16.
[62] Yang N, Tian Y, Zhang M, Peng X, Li F, Li J, et al. Photocatalyst-enzyme hybrid systems for light-driven biotransformation. Biotechnol Adv 2022;54:107808.
[63] Yau MCM, Hayes M, Kalathil S. Biocatalytic conversion of sunlight and carbon dioxide to solar fuels and chemicals. RSC Adv 2022;12(26):16396–411.
[64] Mahmoud M, El-Kalliny AS, Squadrito G. Stacked titanium dioxide nanotubes photoanode facilitates unbiased hydrogen production in a solar-driven photoelectrochemical cell powered with a microbial fuel cell treating animal manure wastewater. Energy Convers Manage 2022;254:115225.
[65] Gai P, Yu W, Zhao H, Qi R, Li F, Liu L, et al. Solar-powered organic semiconductor–bacteria biohybrids for co2 reduction into acetic acid. Angew Chem Int Ed 2020;59(18):7224–9.
[66] Kuk SK, Ham Y, Gopinath K, Boonmongkolras P, Lee Y, Lee YW, et al. Continuous 3d titanium nitride nanoshell structure for solar-driven unbiased biocatalytic co2 reduction. Adv Energy Mater 2019;9(25):1900029.
[67] Ye J, Yu J, Zhang Y, Chen M, Liu X, Zhou S, et al. Light-driven carbon dioxide reduction to methane by methanosarcina barkeri-cds biohybrid. Appl Catal B 2019;257:117916.
[68] Karaca AE, Dincer I. Design and experimental investigation of a new photoelectrochemical reactor for green hydrogen production. Chem Eng Sci 2023;265:118181.
[69] Kobayashi K, Lou SN, Takatsuji Y, Haruyama T, Shimizu Y, Ohno T. Photoelectrochemical reduction of co2 using a tio2 photoanode and a gas diffusion electrode modified with a metal phthalocyanine catalyst. Electrochim Acta 2020;338:135805.
[70] Tahir M, Amin NS. Photocatalytic co2 reduction and kinetic study over in/tio2 nanoparticles supported microchannel monolith photoreactor. Appl Catal A: General 2013;467:483–96.
[71] Fabian DM, Hu S, Singh N, Houle FA, Hisatomi T, Domen K, et al. Particle suspension reactors and materials for solar-driven water splitting. Energy Environ Sci 2015;8(10):2825–50.
[72] Tahir B, Tahir M, Amin NAS. Tailoring performance of la-modified tio2 nanocatalyst for continuous photocatalytic co2 reforming of ch4 to fuels in the presence of h2o. Energy Convers Manage 2018;159:284–98.

[73] Akhundi A, Habibi-Yangjeh A, Abitorabi M, Rahim Pouran S. Review on photocatalytic conversion of carbon dioxide to value-added compounds and renewable fuels by graphitic carbon nitride-based photocatalysts. Catal Rev 2019;61(4):595–628.
[74] Sahani S, Tripathi KM, Lee TI, Dubal DP, Wong C-P, Sharma YC, et al. Recent advances in photocatalytic carbon-based materials for enhanced water splitting under visible-light irradiation. Energy Convers Manage 2022;252:115133.
[75] Limburg B, Bouwman E, Bonnet S. Rate and stability of photocatalytic water oxidation using [ru (bpy) 3] 2+ as photosensitizer. ACS Catal 2016;6(8):5273–84.
[76] Pannwitz A, Klein DM, Rodríguez-Jiménez S, Casadevall C, Song H, Reisner E, et al. Roadmap towards solar fuel synthesis at the water interface of liposome membranes. Chem Soc Rev 2021;50(8):4833–55.
[77] Graetzel M. Artificial photosynthesis: water cleavage into hydrogen and oxygen by visible light. Acc Chem Res 1981;14(12):376–84.
[78] He L, Luo C, Hou Y, Li C, Zhou Q, Sun Y, et al. The effects of micellar media on the photocatalytic h2 production from water. Int J Hydrogen Energy 2011;36(17):10593–9.
[79] Ran J, Jaroniec M, Qiao S-Z. Cocatalysts in semiconductor-based photocatalytic co2 reduction: achievements, challenges, and opportunities. Adv Mater 2018;30(7):1704649.
[80] Luo Y-H, Dong L-Z, Liu J, Li S-L, Lan Y-Q. From molecular metal complex to metal–organic framework: The co2 reduction photocatalysts with clear and tunable structure. Coord Chem Rev 2019;390:86–126.
[81] Hori H, Ishitani O, Koike K, Johnson FP, Ibusuki T. Efficient carbon dioxide photoreduction by novel metal complexes and its reaction mechanisms. Energy Convers Manage 1995;36(6–9):621–4.
[82] Wang S, Hori T. Oxygen evolution sensitized by tin porphyrin in micro-heterogeneous system and membrane systems. J Porphyr Phthalocyanines 2003;7(01):37–41.
[83] Leung C-F, Lau T-C. Organic photosensitizers for catalytic solar fuel generation. Energy & Fuels 2021;35(23):18888–99.
[84] Rao H, Schmidt LC, Bonin J, Robert M. Visible-light-driven methane formation from co2 with a molecular iron catalyst. Nature 2017;548(7665):74–7.
[85] Arias-Rotondo DM, McCusker JK. The photophysics of photoredox catalysis: a roadmap for catalyst design. Chem Soc Rev 2016;45(21):5803–20.
[86] Amao Y, Tomonou Y, Okura I. Highly efficient photochemical hydrogen production system using zinc porphyrin and hydrogenase in ctab micellar system. Sol Energy Mater Sol Cells 2003;79(1):103–11.
[87] Hansen M, Troppmann S, König B. Artificial photosynthesis at dynamic self-assembled interfaces in water. Chem Eur J 2016;22(1):58–72.
[88] Sebata S, y. Takizawa S, Ikuta N, Murata S. Photofunctions of iridium (iii) complexes in vesicles: long-lived excited states and visible-light sensitization for hydrogen evolution in aqueous solution. Dalton Trans 2019;48(39):14914–25.
[89] Rodriguez-Jimenez S, Song H, Lam E, Wright D, Pannwitz A, Bonke SA, et al. Self-assembled liposomes enhance electron transfer for efficient photocatalytic co2 reduction. J Am Chem Soc 2022.
[90] Hu H, Wang Z, Cao L, Zeng L, Zhang C, Lin W, et al. Metal–organic frameworks embedded in a liposome facilitate overall photocatalytic water splitting. Nature Chem 2021;13(4):358–66.
[91] Haussener S, Xiang C, Spurgeon JM, Ardo S, Lewis NS, Weber AZ. Modeling, simulation, and design criteria for photoelectrochemical water-splitting systems. Energy Environ Sci 2012;5(12):9922–35.
[92] Iizuka K, Wato T, Miseki Y, Saito K, Kudo A. Photocatalytic reduction of carbon dioxide over ag cocatalyst-loaded ala4ti4o15 (a= ca, sr, and ba) using water as a reducing reagent. J Am Chem Soc 2011;133(51):20863–8.
[93] Bloh JZ. A holistic approach to model the kinetics of photocatalytic reactions. Front Chem 2019;7:128.
[94] Bjelajac A, Kopač D, Fecant A, Tavernier E, Petrović R, Likozar B, et al. Micro-kinetic modelling of photocatalytic co 2 reduction over undoped and n-doped tio 2. Catal Sci Technol 2020;10(6):1688–98.
[95] Edelmannová M, de los Milagros Ballari M, Přibyl M, Kočí K. Experimental and modelling studies on the photocatalytic generation of hydrogen during water-splitting over a commercial tio2 photocatalyst p25. Energy Convers Manage 2021;245:114582.
[96] Singh MR, Goodpaster JD, Weber AZ, Head-Gordon M, Bell AT. Mechanistic insights into electrochemical reduction of co2 over ag using density functional theory and transport models. Proc Natl Acad Sci 2017;114(42):E8812–21.
[97] Ješić D, Jurković DL, Pohar A, Suhadolnik L, Likozar B. Engineering photocatalytic and photoelectrocatalytic co2 reduction reactions: Mechanisms, intrinsic kinetics, mass transfer resistances, reactors and multi-scale modelling simulations. Chem Eng J 2021;407:126799.
[98] Bohra D, Chaudhry JH, Burdyny T, Pidko EA, Smith WA. Modeling the electrical double layer to understand the reaction environment in a co 2 electrocatalytic system. Energy Environ Sci 2019;12(11):3380–9.
[99] Zhu B, Cheng B, Zhang L, Yu J. Review on dft calculation of s-triazine-based carbon nitride. Carbon Energy 2019;1(1):32–56.
[100] Kovacic Z, Likozar B, Hus M. Photocatalytic co2 reduction: A review of ab initio mechanism, kinetics, and multiscale modeling simulations. ACS Catal 2020;10(24):14984–5007.
[101] Bhatt MD, Lee JS. Recent theoretical progress in the development of photoanode materials for solar water splitting photoelectrochemical cells. J Mater Chem A 2015;3(20):10632–59.
[102] Motagamwala AH, Dumesic JA. Microkinetic modeling: a tool for rational catalyst design. Chem Rev 2020;121(2):1049–76.
[103] Dattila F, Seemakurthi RR, Zhou Y, López N. Modeling operando electrochemical co2 reduction. Chem Rev 2022;122(12):11085–130.
[104] Liu T, Tyburski R, Wang S, Fernandez-Teran R, Ott S, Hammarstrom L. Elucidating proton-coupled electron transfer mechanisms of metal hydrides with free energy-and pressure-dependent kinetics. J Am Chem Soc 2019;141(43):17245–59.
[105] Xie W, Xu J, Chen J, Wang H, Hu P. Achieving theory–experiment parity for activity and selectivity in heterogeneous catalysis using microkinetic modeling. Acc Chem Res 2022;55(9):1237–48.
[106] Lookman T, Balachandran PV, Xue D, Yuan R. Active learning in materials science with emphasis on adaptive sampling using uncertainties for targeted design. Npj Comput Mater 2019;5(1):21.
[107] Grajciar L, Heard CJ, Bondarenko AA, Polynski MV, Meeprasert J, Pidko EA, Nachtigall P. Towards operando computational modeling in heterogeneous catalysis. Chem Soc Rev 2018;47(22):8307–48.
[108] Patzsch J, Berg B, Bloh JZ. Kinetics and optimization of the photocatalytic reduction of nitrobenzene. Front Chem 2019;7:289.
[109] Wang T, Yang L, Yuan K, Du X, Yang Y. Numerical investigation on photocatalytic co2 reduction by solar energy in double-skin sheet reactor. Energy Convers Manage 2014;87:606–17.
[110] Uner D, Yilmaz B. Elucidating the role of adsorption during artificial photosynthesis: H2o and co2 adsorption isotherms over tio2 reveal thermal effects under uv illumination. Photosynth Res 2022;1–15.
[111] Limburg B, Bouwman E, Bonnet S. Effect of liposomes on the kinetics and mechanism of the photocatalytic reduction of methyl viologen. J Phys Chem B 2016;120(28):6969–75.
[112] Sun C, Xuan Y, Zhang K. A multi-process model for the photocatalytic reduction of co 2. Phys Chem Chem Phys 2022;24(36):22231–40.
[113] Altaf CT, Faraji M, Kumtepe A, Abdullayeva N, Yilmaz N, Karagoz E, et al. Highly efficient 3d-zno nanosheet photoelectrodes for solar-driven water splitting: Chalcogenide nanoparticle sensitization and mathematical modeling. J Alloys Compd 2020;828:154472.
[114] Bou A, Torchio P, Vedraine S, Barakel D, Lucas B, Bernède J-C, et al. Numerical optimization of multilayer electrodes without indium for use in organic solar cells. Sol Energy Mater Sol Cells 2014;125:310–7.
[115] Gao C, Yu H, Zhang L, Zhao Y, Xie J, Li C, et al. Ultrasensitive paper-based photoelectrochemical sensing platform enabled by the polar charge carriers-created electric field. Anal Chem 2020;92(4):2902–6.
[116] Würfel P, Würfel U. Physics of solar cells: from basic principles to advanced concepts. John Wiley & Sons; 2016.
[117] Bard AJ, Faulkner LR, White HS. Electrochemical methods: fundamentals and applications. John Wiley & Sons; 2022.
[118] Kutz M. Handbook of environmental degradation of materials. William Andrew; 2018.
[119] Abderezzak B. Introduction to transfer phenomena in PEM fuel cells. Elsevier; 2018.
[120] Bedoya-Lora FE, Hankin A, Kelsall GH. En route to a unified model for photoelectrochemical reactor optimization. ii–geometric optimization of perforated photoelectrodes. Front Chem Eng 2021;3:749058.
[121] Hankin A, Bedoya-Lora F, Ong C, Alexander J, Petter F, Kelsall G. From millimetres to metres: the critical role of current density distributions in photo-electrochemical reactor design. Energy Environ Sci 2017;10(1):346–60.
[122] Sekizawa FE, Oh-Ishi K, Morikawa T. Photoelectrochemical water-splitting over a surface modified p-type cr 2 o 3 photocathode. Dalton Trans 2020;49(3):659–66.
[123] Sharp ID, Atwater HA, Lewerenz H-J. Integrated solar fuel generators. R Soc Chem 2018.
[124] Newman J, Thomas-Alyea KE. Electrochemical systems. John Wiley & Sons; 2012.
[125] Bui JC, Kim C, King AJ, Romiluyi O, Kusoglu A, Weber AZ, et al. Engineering catalyst–electrolyte microenvironments to optimize the activity and selectivity for the electrochemical reduction of co2 on cu and ag. Acc Chem Res 2022;55(4):484–94.
[126] Gaudy YK, Haussener S. Utilizing modeling, experiments, and statistics for the analysis of water-splitting photoelectrodes. J Mater Chem A 2016;4(8):3100–14.
[127] Berger A, Newman J. An integrated 1-dimensional model of a photoelectrochemical cell for water splitting. J Electrochem Soc 2014;161(8):E3328.
[128] Bui JC, Lees EW, Pant LM, Zenyuk IV, Bell AT, Weber AZ. Continuum modeling of porous electrodes for electrochemical synthesis. Chem Rev 2022.
[129] Njoka F, Mori S, Ookawara S, Ahmed M. Effects of photo-generated gas bubbles on the performance of tandem photoelectrochemical reactors for hydrogen production. Int J Hydrogen Energy 2019;44(21):10286–300.
[130] Bedoya-Lora FE, Hankin A, Kelsall GH. En route to a unified model for photoelectrochemical reactor optimisation. i-photocurrent and h 2 yield predictions. J Mater Chem A 2017;5(43):22683–96.

[131] Vogt H. The rate of gas evolution of electrodes—i. an estimate of the efficiency of gas evolution from the supersaturation of electrolyte adjacent to a gas-evolving electrode. Electrochim Acta 1984;29(2):167–73.
[132] Joe JCK, Janssen L, Van Strelen S, Verbunt J, Sluyter W. Bubble parameters and efficiency of gas bubble evolution for a chlorine-, a hydrogen-and an oxygen-evolving wire electrode. Electrochim Acta 1988;33(6):769–79.
[133] Zhang G, Fan L, Sun J, Jiao K. A 3d model of pemfc considering detailed multiphase flow and anisotropic transport properties. Int J Heat Mass Transfer 2017;115:714–24.
[134] Angulo AE, Frey D, Modestino MA. Understanding bubble-induced overpotential losses in multiphase flow electrochemical reactors. Energy & Fuels 2022;36(14):7908–14.
[135] Rivera FF, Pérez T, Castañeda LF, Nava JL. Mathematical modeling and simulation of electrochemical reactors: A critical review. Chem Eng Sci 2021;239:116622.
[136] Chu F, Li S, Chen H, Yang L, Ola O, Maroto-Valer M, et al. Modeling photocatalytic conversion of carbon dioxide in bubbling twin reactor. Energy Convers Manage 2017;149:514–25.
[137] Qureshy AM, Dincer I. Development of a new solar photoelectrochemical reactor design for more efficient hydrogen production. Energy Convers Manage 2021;228:113714.
[138] Le XT. Permselectivity and microstructure of anion exchange membranes. J Colloid Interface Sci 2008;325(1):215–22.
[139] Salomov UR, Chiavazzo E, Asinari P. Gas-dynamic and electro-chemical optimization of catalyst layers in high temperature polymeric electrolyte membrane fuel cells. Int J Hydrogen Energy 2015;40(15):5425–31.
[140] Zhao W, Pinfield VJ, Wang H, Xuan J, Niu Z. An open source framework for advanced multi-physics and multiscale modelling of solid oxide fuel cells. Energy Convers Manage 2023;280:116791.
[141] Unke OT, Chmiela S, Sauceda HE, Gastegger M, Poltavsky I, Schutt KT, et al. Machine learning force fields. Chem Rev 2021;121(16):10142–86.
[142] Senftle TP, Hong S, Islam MM, Kylasa SB, Zheng Y, Shin YK, et al. The reaxff reactive force-field: development, applications and future directions. Npj Comput Mater 2016;2(1):1–14.
[143] Han Y, Jiang D, Zhang J, Li W, Gan Z, Gu J. Development, applications and challenges of reaxff reactive force field in molecular simulations. Front Chem Sci Eng 2016;10:16–38.
[144] Poltavsky I, Tkatchenko A. Machine learning force fields: Recent advances and remaining challenges. J Phys Chem Lett 2021;12(28):6551–64.
[145] Praprotnik M, Site LD, Kremer K. Multiscale simulation of soft matter: From scale bridging to adaptive resolution. Annu Rev Phys Chem 2008;59:545–71.
[146] Falciani G, Franklin R, Cagna A, Sen I, Hassanali A, Chiavazzo E. A multi-scale perspective of gas transport through soap-film membranes. Molecul Syst Design Eng 2020;5(5):911–21.
[147] Shelley JC, Shelley MY. Computer simulation of surfactant solutions. Curr Opin Colloid Interf Sci 2000;5(1–2):101–10.
[148] Kuhn H, Rehage H. Molecular dynamics computer simulations of surfactant monolayers: Monododecyl pentaethylene glycol at the surface between air and water. J Phys Chem B 1999;103(40):8493–501.
[149] Hashemzadeh H, Javadi H, Darvishi M. Study of structural stability and formation mechanisms in dspc and dpsm liposomes: A coarse-grained molecular dynamics simulation. Sci Rep 2020;10(1):1–10.
[150] Duncan SL, Dalal IS, Larson RG. Molecular dynamics simulation of phase transitions in model lung surfactant monolayers. Biochim Biophys Acta (BBA)-Biomemb 2011;1808(10):2450–65.
[151] Moghimikheirabadi A, Sagis LM, Kröger M, Ilg P. Gas–liquid phase equilibrium of a model langmuir monolayer captured by a multiscale approach. Phys Chem Chem Phys 2019;21(5):2295–306.
[152] Israelachvili JN. Intermolecular and surface forces. Academic Press; 2011.
[153] Nagarajan R. Molecular packing parameter and surfactant self-assembly: the neglected role of the surfactant tail. Langmuir 2002;18(1):31–8.
[154] Stephenson BC, Beers K, Blankschtein D. Complementary use of simulations and molecular-thermodynamic theory to model micellization. Langmuir 2006;22(4):1500–13.
[155] Scholes GD, Fleming GR, Olaya-Castro A, Van Grondelle R. Lessons from nature about solar light harvesting. Nature Chem 2011;3(10):763–74.
[156] Chen H-Y, Ardo S. Direct observation of sequential oxidations of a titania-bound molecular proxy catalyst generated through illumination of molecular sensitizers. Nature Chem 2018;10(1):17–23.
[157] Klein DM, Passerini L, Huber M, Bonnet S. A stable alkylated cobalt catalyst for photocatalytic h2 generation in liposomes. ChemCatChem 2022;14(20):e202200484.
[158] Ageeva TA, Bush AA, Golubev DV, Gorshkova AS, Kamentsev KE, Koifman OI, et al. Porphyrin metal complexes with a large dipole moment. J Organomet Chem 2020;922:121355.
[159] Adachi M, Yoneyama M, Nakamura S. Pressure-induced changes in the absorption spectrum of monolayers at the air/water interface: Comparison of calculations with experiments. Langmuir 1992;8(9):2240–6.
[160] Gonçalves da Silva AM, Viseu MI, Malathi A, Antunes P, Costa SM. Organization of meso-tetra (4-n-stearylpyridyl) porphine in pure and mixed monolayers at the air/water interface and in langmuir- blodgett films. Langmuir 2000;16(3):1196–204.
[161] Choudhury B, Weedon AC, Bolton JR. Effects of molecular organization on photophysical behavior. 1. steady-state fluorescence and fluorescence quantum yield studies of langmuir- blodgett monolayers of some surfactant porphyrins. Langmuir 1998;14(21):6192–8.
[162] Ghosh A, Mahato P, Choudhury S, Das A. Comparative study of porphyrin derivatives in monolayers at the air–water interface and in langmuir–blodgett films. Thin Solid Films 2011;519(22):8066–73.
[163] Viseu MI, Gonçalves da Silva AM, Antunes P, Costa SM. Organization of cationic porphyrins in mixed langmuir- blodgett films. an absorption and steady-state fluorescence study. Langmuir 2002;18(15):5772–81.
[164] Joshi SY, Deshmukh SA. A review of advancements in coarse-grained molecular dynamics simulations. Mol Simul 2021;47(10–11):786–803.
[165] Liguori N, Croce R, Marrink SJ, Thallmair S. Molecular dynamics simulations in photosynthesis. Photosynth Res 2020;144(2):273–95.
[166] Brini E, Algaer EA, Ganguly P, Li C, Rodríguez-Ropero F, van der Vegt NF. Systematic coarse-graining methods for soft matter simulations–a review. Soft Matter 2013;9(7):2108–19.
[167] Marrink SJ, Risselada HJ, Yefimov S, Tieleman DP, De Vries AH. The martini force field: coarse grained model for biomolecular simulations. J Phys Chem B 2007;111(27):7812–24.
[168] Groot RD, Warren PB. Dissipative particle dynamics: Bridging the gap between atomistic and mesoscopic simulation. J Chem Phys 1997;107(11):4423–35.
[169] Gera R, Bakker HJ, Franklin-Mergarejo R, Morzan UN, Falciani G, Bergamasco L, et al. Emergence of electric fields at the water–c12e6 surfactant interface. J Am Chem Soc 2021;143(37):15103–12.
[170] Lopez CF, Moore PB, Shelley JC, Shelley MY, Klein ML. Computer simulation studies of biomembranes using a coarse grain model. Comput Phys Comm 2002;147(1–2):1–6.
[171] Orsi M, Haubertin DY, Sanderson WE, Essex JW. A quantitative coarse-grain model for lipid bilayers. J Phys Chem B 2008;112(3):802–15.
[172] Ruiz-Morales Y, Romero-Martinez A. Coarse-grain molecular dynamics simulations to investigate the bulk viscosity and critical micelle concentration of the ionic surfactant sodium dodecyl sulfate (sds) in aqueous solution. J Phys Chem B 2018;122(14):3931–43.
[173] Timounay Y, Pannwitz A, Klein DM, Biance A-L, Hoefnagel ME, Sen I, et al. Interfacial characterization of ruthenium-based amphiphilic photosensitizers. Langmuir 2022;38(31):9697–707.
[174] Eric V, Li X, Dsouza L, Frehan SK, Huijser A, Holzwarth AR, et al. Manifestation of hydrogen bonding and exciton delocalization on the absorption and two-dimensional electronic spectra of chlorosomes. J Phys Chem B 2023.
[175] Jambeck JP, Eriksson ES, Laaksonen A, Lyubartsev AP, Eriksson LA. Molecular dynamics studies of liposomes as carriers for photosensitizing drugs: development, validation, and simulations with a coarse-grained model. J Chem Theory Comput 2014;10(1):5–13.
[176] Tavernelli I, Curchod BF, Rothlisberger U. Nonadiabatic molecular dynamics with solvent effects: A lr-tddft qm/mm study of ruthenium (ii) tris (bipyridine) in water. Chem Phys 2011;391(1):101–9.
[177] Wang S-p, Huang X, He Y, Zhang H, Zhou J, Tang G, et al. Amphiphilic porphyrin-based supramolecular self-assembly for photochemotherapy: From molecular design to application. Nano Today 2023;48:101732.
[178] Liu K, Kang Y, Ma G, Möhwald H, Yan X. Molecular and mesoscale mechanism for hierarchical self-assembly of dipeptide and porphyrin light-harvesting system. Phys Chem Chem Phys 2016;18(25):16738–47.
[179] Nikoloudakis E, López-Duarte I, Charalambidis G, Ladomenou K, Ince M, Coutsolelos AG. Porphyrins and phthalocyanines as biomimetic tools for photocatalytic h 2 production and co 2 reduction. Chem Soc Rev 2022.
[180] Sai H, Erbas A, Dannenhoffer A, Huang D, Weingarten A, Siismets E, et al. Chromophore amphiphile–polyelectrolyte hybrid hydrogels for photocatalytic hydrogen production. J Mater Chem A 2020;8(1):158–68.
[181] Falciani G, Bergamasco L, Bonke SA, Sen I, Chiavazzo E. A novel concept of photosynthetic soft membranes: a numerical study. Nanoscale Res Lett 2023;18(1):9.
[182] Tadros TF. An introduction to surfactants. In: An introduction to surfactants. de Gruyter; 2014.
[183] Butt H-J, Graf K, Kappl M. Physics and chemistry of interfaces. John Wiley & Sons; 2013.
[184] Ivanov IB, Danov KD, Dimitrova D, Boyanov M, Ananthapadmanabhan KP, Lips A. Equations of state and adsorption isotherms of low molecular non-ionic surfactants. Colloids Surf A 2010;354(1–3):118–33.
[185] Broze G. Handbook of detergents, part a: properties. CRC Press; 1999.
[186] Puvvada S, Blankschtein D. Molecular-thermodynamic approach to predict micellization, phase behavior and phase separation of micellar solutions. i. application to nonionic surfactants. J Chem Phys 1990;92(6):3710–24.
[187] Mulqueen M, Blankschtein D. Prediction of equilibrium surface tension and surface adsorption of aqueous surfactant mixtures containing ionic surfactants. Langmuir 1999;15(26):8832–48.

[188] Kralchevsky P, Danov K, Kolev V, Broze G, Mehreteab A. Effect of nonionic admixtures on the adsorption of ionic surfactants at fluid interfaces. 1. sodium dodecyl sulfate and dodecanol. Langmuir 2003;19(12):5004–18.
[189] Karakashev SI, Manev ED. Effect of interactions between the adsorbed species on the properties of single and mixed-surfactant monolayers at the air/water interface. J Colloid Interface Sci 2002;248(2):477–86.
[190] Fainerman V, Lucassen-Reynders E, Miller R. Adsorption of surfactants and proteins at fluid interfaces. Colloids Surf A 1998;143(2–3):141–65.
[191] Fainerman V, Vollhardt D. Equations of state for langmuir monolayers with two-dimensional phase transitions. J Phys Chem B 1999;103(1):145–50.
[192] Fainerman V, Vollhardt D. Penetration of langmuir monolayers by soluble amphiphilic molecules. Langmuir 1999;15(5):1784–90.
[193] Liu M, Pang Y, Zhang B, De Luna P, Voznyy O, Xu J, et al. Enhanced electrocatalytic co2 reduction via field-induced reagent concentration. Nature 2016;537(7620):382–6.
[194] Iozzo DA, Tong M, Wu G, Furlani EP. Numerical analysis of electric double layer capacitors with mesoporous electrodes: effects of electrode and electrolyte properties. J Phys Chem C 2015;119(45):25235–42.
[195] Torrie G, Valleau J. Electrical double layers. i. monte carlo study of a uniformly charged surface. J Chem Phys 1980;73(11):5807–16.
[196] Giera B, Henson N, Kober EM, Shell MS, Squires TM. Electric double-layer structure in primitive model electrolytes: comparing molecular dynamics with local-density approximations. Langmuir 2015;31(11):3553–62.
[197] Glosli JN, Philpott MR. Molecular dynamics simulation of adsorption of ions from aqueous media onto charged electrodes. J Chem Phys 1992;96(9):6962–9.
[198] Valleau JP, Cohen LK. Primitive model electrolytes. i. grand canonical monte carlo computations. J Chem Phys 1980;72(11):5935–41.
[199] Valiskó M, Kristóf T, Gillespie D, Boda D. A systematic monte carlo simulation study of the primitive model planar electrical double layer over an extended range of concentrations, electrode charges, cation diameters and valences. AIP Adv 2018;8(2):025320.
[200] Fahrenberger F, Xu Z, Holm C. Simulation of electric double layers around charged colloids in aqueous solution of variable permittivity. J Chem Phys 2014;141(6):064902.
[201] Larsen AH, Mortensen JJ, Blomqvist J, Castelli IE, Christensen R, Dułak M, et al. The atomic simulation environment—a python library for working with atoms. J Phys: Condens Matter 2017;29(27):273002.
[202] Wilkinson MD, Dumontier M, Aalbersberg IJ, Appleton G, Axton M, Baak A, et al. The fair guiding principles for scientific data management and stewardship. Sci Data 2016;3(1):1–9.
[203] Chiavazzo E, Covino R, Coifman RR, Gear CW, Georgiou AS, Hummer G, et al. Intrinsic map dynamics exploration for uncharted effective free-energy landscapes. Proc Natl Acad Sci 2017;114(28):E5494–503.
[204] Arnarez C, Uusitalo JJ, Masman MF, Ingólfsson HI, De Jong DH, Melo MN, et al. Arrink, dry martini, a coarse-grained force field for lipid membrane simulations with implicit solvent. J Chem Theory Comput 2015;11(1):260–75.
[205] Fasano M, Falciani G, Brancato V, Palomba V, Asinari P, Chiavazzo E, et al. Atomistic modelling of water transport and adsorption mechanisms in silicoaluminophosphate for thermal energy storage. Appl Therm Eng 2019;160:114075.
[206] De Angelis P, Cappabianca R, Fasano M, Asinari P, Chiavazzo E. Enhancing reaxff for molecular dynamics simulations of lithium-ion batteries: An interactive reparameterization protocol. 2023, arXiv preprint arXiv:2306.13027.
[207] Chiavazzo E, Karlin I. Adaptive simplification of complex multiscale systems. Phys Rev E 2011;83(3):036706.
[208] Chiavazzo E. Approximation of slow and fast dynamics in multiscale dynamical systems by the linearized relaxation redistribution method. J Comput Phys 2012;231(4):1751–65.
[209] Chiavazzo E, Gear CW, Dsilva CJ, Rabin N, Kevrekidis IG. Reduced models in chemical kinetics via nonlinear data-mining. Processes 2014;2(1):112–40.
[210] MacLeod BP, Parlane FG, Brown AK, Hein JE, Berlinguette CP. Flexible automation accelerates materials discovery. Nature Mater 2022;21(7):722–6.
[211] Bai Y, Wilbraham L, Slater BJ, Zwijnenburg MA, Sprick RS, Cooper AI. Accelerated discovery of organic polymer photocatalysts for hydrogen evolution from water through the integration of experiment and theory. J Am Chem Soc 2019;141(22):9063–71.
[212] Trezza G, Bergamasco L, Fasano M, Chiavazzo E. Minimal crystallographic descriptors of sorption properties in hypothetical mofs and role in sequential learning optimization. Npj Comput Mater 2022;8(1):123.
[213] Trezza G, Chiavazzo E. Leveraging composition-based material descriptors for machine learning optimization. 2023, arXiv preprint arXiv:2304.07592.
[214] Raccuglia P, Elbert KC, Adler PD, Falk C, Wenny MB, Mollo A, et al. Machine-learning-assisted materials discovery using failed experiments. Nature 2016;533(7601):73–6.
[215] Falciani G, Chiavazzo E. Grand canonical monte carlo code for simulating ions distribution close to a charged surface. 2023, http://dx.doi.org/10.5281/zenodo.7802655.
[216] Falciani G, Chiavazzo E. Gran canonical monte carlo algorithm to calculate the distribution of ions close to a charged planar surface. 2023, URL https://github.com/gabfuni/GCMC_ions.